Redox Biology 71 (2024) 103119

Contents lists available at ScienceDirect

Redox Biology

journal homepage: www.elsevier.com/locate/redox

Hybrid molecules synergistically mitigate ferroptosis and amyloid-associated toxicities in Alzheimer's disease

Dikshaa Padhi, Prayasee Baruah, Madhu Ramesh, Hariharan Moorthy, Thimmaiah Govindaraju *

Bioorganic Chemistry Laboratory, New Chemistry Unit, Jawaharlal Nehru Centre for Advanced Scientific Research, Bengaluru, Karnataka, 560064, India

ARTICLE INFO

Keywords:
Alzheimer's disease
Ferroptosis
Glutathione peroxidase 4
Liquid-liquid phase separation
Hybrid molecules

ABSTRACT

Alzheimer's disease (AD) is a neurodegenerative disorder characterized by the build-up of extracellular amyloid β (Aβ) plaques and intracellular neurofibrillary tangles (NFTs). Ferroptosis, an iron (Fe)-dependent form of cell death plays a significant role in the multifaceted AD pathogenesis through generation of reactive oxygen species (ROS), mitochondrial damage, lipid peroxidation, and reduction in glutathione peroxidase 4 (GPX4) enzyme activity and levels. Aberrant liquid-liquid phase separation (LLPS) of tau drives the growth and maturation of NFTs contributing to AD pathogenesis. In this study, we strategically combined the structural and functional properties of gallic acid (GA) and cyclic dipeptides (CDPs) to synthesize hybrid molecules that effectively target both ferroptosis and amyloid toxicity in AD. This innovative approach marks a paradigm shift from conventional therapeutic strategies. This is the first report of a synthetic small molecule (**GCTR**) that effectively combats ferroptosis, simultaneously restoring enzymatic activity and enhancing cellular levels of its master regulator, GPX4. Further, **GCTR** disrupts Fe^{3+}-induced LLPS of tau, and aids in attenuation of abnormal tau fibrillization. The synergistic action of **GCTR** in combating both ferroptosis and amyloid toxicity, bolstered by GPX4 enhancement and modulation of Fe^{3+}-induced tau LLPS, holds promise for the development of small molecule-based novel therapeutics for AD.

1. Introduction

Alzheimer's disease (AD) is a major neurodegenerative disorder and a significant contributor to dementia [1–3]. It affects millions of people worldwide, manifesting as clinical deficit in learning and memory, as well as cognitive decline. AD is pathologically characterised by the deposition of extracellular Aβ plaques, intracellular NFTs of tau and associated neurodegeneration. Redox active metal ions such as, Fe^{3+} and Cu^{2+}, and in their Aβ bound states can catalyse ROS production, leading to oxidative damage, accelerated Aβ aggregation, and neuro-inflammation, ultimately contributing to neurotoxicity in AD [4,5]. Specifically, Fe dyshomeostasis accelerates Aβ plaque formation and tau aggregation, exacerbating their toxic effects and fostering AD development [6]. Increased Fe^{3+} levels contribute to tau aggregation through hyperphosphorylation and by facilitating LLPS of tau, leading to NFTs [7,8]. Small molecules, natural products, and polymer-based inhibitors have shown potential in modulating tau fibrillization, while targeting Fe^{3+}-induced LLPS of tau is an emerging approach [9–11].

Transferrin (Tf) plays a crucial role in intracellular transport of both Fe^{2+} and Fe^{3+} to various biological tissues, facilitating their distribution and utilization [12,13]. Fe^{3+} undergoes Fenton reaction in the presence of hydrogen peroxide (H_2O_2) generating excess ROS. This cascade of events leads to DNA damage, lipid peroxidation, and mitochondrial damage, collectively contributing to oxidative stress, inflammation, and neuronal death in AD [14]. Accumulation of Fe in the brain triggers a series of pathological processes, ultimately culminating in ferroptosis [15]. In principle, ferroptosis/oxytosis, a Fe-dependent cell death mechanism, has interconnected pathways in AD [16–18]. Cells rely on their innate defence mechanisms, with GPX4 as a pivotal player, to mitigate the detrimental effects of ferroptosis, such as lipid peroxidation [19,20]. GPX4 mitigates lipid hydroperoxides (LOOH) by catalysing their conversion into lipid alcohols using glutathione (GSH) as a

Abbreviations: AD, Alzheimer's disease; Aβ, amyloid β; GPX4, glutathione peroxidase 4; LLPS, liquid-liquid phase separation; GA, Gallic acid; CDPs, cyclic dipeptides.

* Corresponding author.
E-mail address: tgraju@jncasr.ac.in (T. Govindaraju).

https://doi.org/10.1016/j.redox.2024.103119
Received 21 January 2024; Received in revised form 22 February 2024; Accepted 7 March 2024
Available online 11 March 2024
2213-2317/© 2024 The Authors. Published by Elsevier B.V. This is an open access article under the CC BY-NC license (http://creativecommons.org/licenses/by-nc/4.0/).

co-factor. In doing so, it acts as a crucial regulator that prevents Fe-dependent formation of toxic lipid ROS [21]. In addition to GPX4, other key players in the regulation of Fe^{3+} levels and the control of ferroptosis include Ferroptosis Suppressor Protein 1 (FSP1), Ferritin and Ferroportin (FPN) [22,23]. The intricate dynamics of Fe^{3+} accumulation, GSH depletion, reduced GPX4 activity and levels, and generation of LOOH predispose cells to ferroptosis. This characteristic pattern is notably observed in the brains of patients diagnosed with AD [24]. Therefore, targeting ferroptotic mechanisms holds promise for viable therapeutic interventions against both ferroptosis and AD [25].

Polyphenols like gallic acid (GA) and its derivatives are studied for metal chelation, antioxidant, anti-inflammatory, $A\beta_{42}$ aggregation inhibition, and neuroprotective properties [26–28]. Additionally, CDPs are a promising category of biologically active compounds, highly regarded for their antioxidant, anti-inflammatory, and neuroprotective properties [29]. Furthermore, their potential as brain shuttles for drug delivery is of significant interest [30,31]. The enhanced structural rigidity, molecular recognition and biocompatibility of CDPs make them attractive pharmacophores [9,32,33]. We rationally designed and synthesized hybrid molecules by strategically integrating the structural and functional features of GA and CDPs to enhance their multifunctional therapeutic properties [34]. In this study, GA was functionalized with CDPs derived from L-phenylalanine, L-tyrosine, L-tryptophan, and L-dopa, in combination with L-lysine, to obtain GA-CDP hybrid molecules (**GCPH**, **GCTY**, **GCTR**, and **GCLD**) (Scheme 1). These hybrids were strategically developed to target ferroptosis as well as Fe-dependent and independent amyloid toxicity in AD. Among the hybrids, **GCTR** demonstrated superior performance in terms of Fe-chelation and effectively inhibited the aggregation of $A\beta_{42}/A\beta_{42}+Fe^{3+}$, the excess ROS production, and cytotoxicity. Notably, **GCTR** inhibited Fe^{3+}-induced LLPS of tau, its aggregation and associated toxicity. **GCTR** rescued SH-SY5Y cells from RAS-selective lethal 3((1S,3R)-RSL3)-induced ferroptosis, prevented mitochondrial damage, and alleviated lipid peroxidation. Remarkably, **GCTR** not only restored the enzymatic activity but also enhanced the cellular levels of GPX4, thereby positioning itself as a potential inhibitor of ferroptosis. To the best of our knowledge, this represents an innovative approach to simultaneously target $Fe^{3+}/A\beta_{42}+Fe^{3+}$-induced ferroptosis and amyloid toxicity in AD using synthetic small hybrid molecules (Fig. 1).

2. Materials and methods

2.1. Materials and reagents

Solvents and reagents were procured from Merck or Spectrochem and were used without further purification, unless otherwise specified. Protein expression and purification materials were obtained from HiMedia or Invitrogen, following the manufacturers' instructions. The Glutathione Peroxidase Assay Kit was purchased from Cayman Chemicals (Item No. 703102). 2,2-diphenyl-1-picrylhydrozyl (DPPH), 3-(4,5-dimethylthiazol-2-yl)-2,5 diphenyltetrazolium bromide (MTT), metal salts ($FeCl_3$), thiobarbituric acid (TBA), butylated hydroxytoluene (BHT), and Atto 647 N-Nitrilotriacetic acid complexed to Ni^{2+} (NTA-Atto 647-N) were obtained from Merck Millipore, used without additional purification. Isothermal titration calorimetry (ITC) measurements were conducted using a Malvern MicroCal-PEAQ ITC instrument. Absorbance and fluorescence readings in well plates were recorded with a Spectramax i3 (Molecular Devices) plate reader. Immunofluorescence studies were carried out using an Olympus Fluoview-3000 confocal laser scanning microscope and Leica Dmi8 fluorescent microscope with live cell imaging setup and analysed using ImageJ software. Dynamic light scattering (DLS) measurements for determining hydrodynamic diameter and zeta potential were performed with a Malvern Nano series light scattering instrument. Data analysis and plotting were carried out using Origin (Pro) Version 2022, and GraphPad Prism 8.0.1 software. Molecular docking studies were performed using AutoDock Vina 2.0 and UCSF Chimera, and residual analysis of docked poses was conducted using Discovery Studio Visualizer (DSV).

2.2. Design and chemical synthesis

Rationally designed GA-CDP hybrids (**GCPH**, **GCTY**, **GCTR** and **GCLD**) were prepared by following the synthetic route shown in Scheme 1 $^{\varepsilon}$N-Boc, $^{\alpha}$N-Boc-Lys-OH and respective amino acid esters were coupled using standard solution phase peptide coupling conditions to yield precursor dipeptides, εN-Boc, αN-Boc-Lys-(amino acid)-OMe (**1a-d**). The dipeptides **1a-d** (3.9 g, 7.69 mmol) were treated with formic acid (30 mL) for Boc deprotection and allowed to stir at room temperature for 3 h and monitored using thin layer chromatography (TLC). After completion of the reaction, as confirmed by TLC, formic acid was evaporated under reduced pressure, followed by co-evaporation with toluene (2 x 20 mL). The obtained residue was dried under a vacuum for 30 min and subjected to cyclization in sec-butanol (75 mL, 50 mM) under reflux

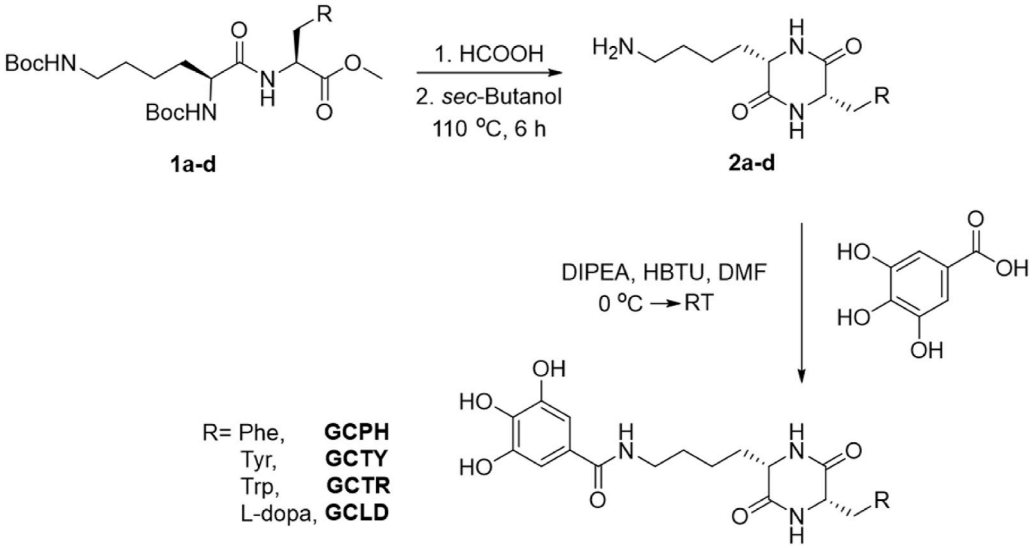

Scheme 1. Synthesis of GA-CDP hybrids (**GCPH**, **GCTY**, **GCTR**, **GCLD**).

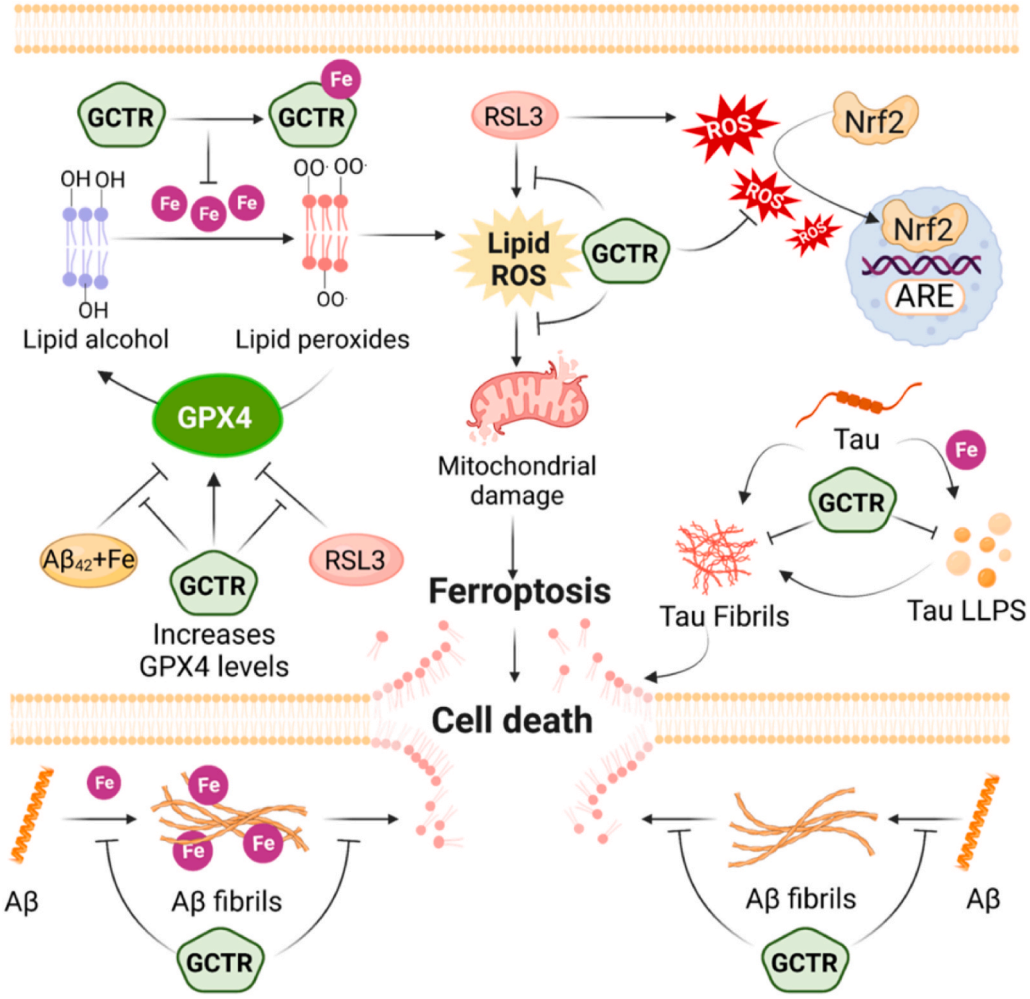

Fig. 1. Schematic shows the mechanism of action of **GCTR** in combating ferroptosis and amyloid toxicity in AD. **GCTR** chelates Fe^{3+}, inhibits $A\beta_{42}$/$A\beta_{42}$+Fe^{3+} aggregation and associated toxicity, Fe^{3+}-induced LLPS of tau and its aggregation, and lipid peroxidation. **GCTR** restores Nrf2 homeostasis, mitigates mitochondrial damage, and enhances GPX4 cellular levels. LLPS: Liquid-liquid phase separation, GPX4: Glutathione Peroxidase 4, ROS: Reactive Oxygen Species, Nrf2: Nuclear factor erythroid 2–related factor 2, RSL3: RAS-selective lethal 3 (Created with BioRender.com).

conditions at 110 °C until the formation of a white precipitate was observed [9,29,35].

The reaction mixture was evaporated to remove ~70% solvent under reduced pressure in a rotary evaporator, followed by filtration using a sintered funnel and washing with dichloromethane (DCM) to obtain the CDPs (**2a-d**). The amine functionality of CDPs (**2a-d**) was subsequently coupled with GA (163.32 mg, 0.96 mmol) using HBTU coupling reagent, and DIPEA as base in DMF, and allowed to stir for 16 h at 0 °C to RT. The purity of the obtained GA-CDP hybrids was monitored by thin layer chromatography (TLC), followed by evaporation of volatiles under reduced pressure. All the GA-CDP hybrids were purified by column chromatography and the integrity of the final compounds was ascertained by ^{1}H NMR, ^{13}C NMR, HR-MS, and LC-MS analysis.

GCPH. Yield 71% (154 mg); colourless solid $R_{f=}$0.5 (MeOH/DCM = 0.5:9.5) ^{1}H NMR (400 MHz, DMSO-d_6) δ_{ppm} 8.13 (s, 1H), 8.04 (s, 1H), 7.92 (s, 1H), 7.24 (s, 2H), 7.22 (s, 2H), 7.15 (s, 2H), 7.09 (dt, J = 5.2, 2.5 Hz, 1H), 7.07 (s, 1H), 6.90 (s, 1H), 6.79 (s, 1H), 4.17 (s, 1H), 3.55 (s, 1H), 3.14 (s, 1H), 2.97 (s, 2H), 2.85 (s, 1H), 1.17 (s, 2H), 1.06 (s, 2H), 0.76 (s, 2H). ^{13}C NMR (100 MHz, DMSO-d_6) ^{13}C NMR (101 MHz) δ_{ppm} 167.6, 166.7, 14.3, 146.0, 136.7, 130.9, 128.5, 127.2, 125.7, 109.3, 107.2, 55.9, 54.4, 38.7, 33.7, 29.4, 29.1, 21.8. HRMS (ESI-MS): m/z calcd for $C_{22}H_{24}N_3O_6$ $[M-H]^+$ 426.1665, found 426.1670.

GCTY. Yield 76% (175 mg); colourless solid $R_{f=}$0.4 (MeOH/DCM = 0.5:9.5) ^{1}H NMR (400 MHz, DMSO-d_6) δ_{ppm} 8.46 (s, 2H), 8.11 (s, 2H), 8.00 (s, 2H), 6.91 (d, J = 8.4 Hz, 4H), 6.65 (d, J = 8.3 Hz, 4H), 4.09 (s, 2H), 3.53 (s, 2H), 3.05 (d, J = 10.5 Hz, 2H), 2.69 (d, J = 13.6 Hz, 2H), 2.55 (s, 3H), 1.26 (s, 3H), 1.00 (s, 1H), 0.77 (s, 4H), 0.61 (s, 2H). ^{13}C NMR (101 MHz) δ_{ppm} 167.0, 156.8, 131.3, 125.5, 114.8, 55.5, 53.7, 37.2, 33.0, 27.3, 20.9. HRMS (ESI-MS): m/z calcd for $C_{22}H_{24}N_3O_7$ $[M-H]^+$ 442.1624, found 442.1644.

GCTR. Yield 73% (185 mg); colourless solid $R_{f=}$0.4 (MeOH/DCM = 0.5:9.5) ^{1}H NMR (400 MHz, DMSO-d_6) δ_{ppm} 10.89 (s, 3H), 8.09 (d, J = 11.4 Hz, 3H), 7.94 (s, 4H), 7.83 (d, J = 11.7 Hz, 1H), 7.73 (d, J = 7.3 Hz, 2H), 7.57 (s, 3H), 7.51 (d, J = 7.4 Hz, 3H), 7.29 (s, 3H), 7.20 (s, 4H), 7.05 (s, 6H), 6.91 (s, 6H), 4.13 (s, 3H), 3.25 (s, 5H), 3.02 (s, 3H), 2.98 (s, 2H), 2.77 (s, 5H), 1.10 (s, 4H), 0.97 (s, 6H), 0.55 (s, 7H). ^{13}C NMR (101 MHz) δ_{ppm} 168.2, 161.3, 146.0, 143.5, 138.5, 136.5, 128.5, 125.3, 124.2, 123.4, 121.3, 118.8, 111.4, 109.2, 55.9, 54.4, 44.5, 37.4, 33.6, 29.2, 21.5, 19.2. HRMS (ESI-MS): m/z calcd for $C_{24}H_{25}N_4O_6$ $[M-H]^+$ 465.1810, found 465.1800.

GCLD. Yield 62% (154 mg); colourless solid $R_{f=}$0.3 (MeOH/DCM = 0.5:9.5) ^{1}H NMR (400 MHz, DMSO-d_6) δ_{ppm} 8.13 – 7.92 (m, 12H), 7.73 (d, J = 9.8 Hz, 4H), 7.52 (d, J = 8.0 Hz, 5H), 7.22 (d, J = 18.2 Hz, 7H), 6.91 (s, 15H), 6.59 (s, 9H), 6.39 (d, J = 8.0 Hz, 3H), 6.32 (s, 3H), 4.09 (d, J = 29.7 Hz, 6H), 3.56 (s, 7H), 2.90 (s, 10H), 2.87 (s, 15H), 2.53 (s, 7H), 1.29 (s, 11H), 1.19 (s, 6H), 1.17 – 1.07 (m, 9H), 0.81 (s, 12H). ^{13}C NMR (101 MHz) δ_{ppm} 168.2, 161.4, 146.0, 138.5, 124.5, 124.0, 123.9, 121.1, 118.6, 115.7, 111.6, 109.3, 107.2, 56.1, 54.0, 44.7, 35.0, 33.6, 29.3,

21.3. HRMS (ESI-MS): *m/z* calcd. for $C_{24}H_{25}N_4O_6$ $[M + NH_4]^+$ 477.2785, found 477.2796.

2.3. Cell culture

SH-SY5Y cells were grown in Dulbecco's modified Eagle medium (DMEM, Cat# MT-10-013-CV, Thermo Fisher Scientific, Waltham, MA) supplemented with 10% fetal bovine serum (FBS, Cat# 26140-079, Gibco), and 1% Penicillin-Streptomycin (PS, 10,000 U/mL, lCat#15140122), and cells were grown at 37 °C with 5% CO_2 atmosphere for 24 h. Sterile T25 flasks (Eppendorf), 96-well plates (Thermo Fischer Scientific), and confocal dishes (SPL Lifesciences) were procured and used without further sterilization.

2.4. Photophysical studies

UV–visible spectroscopy was carried out using single beam Agilent 8453 UV–Vis spectrophotometer at room temperature. Quartz cuvette of 1 cm path length (1 mL) was used for the absorbance measurement (200-800 nm). Freshly prepared 10 mM stock solutions of the GA-CDP hybrids were prepared in DMSO. The Fe^{3+}-binding properties of GA-CDP hybrids were carried out in phosphate buffered saline (PBS) buffer (10 mM, pH = 7.4). Increasing concentrations of Fe^{3+} (0 to 15 μM) were titrated into the compound solutions, with 5 min incubation after each addition, and recorded the changes in absorbance spectra. The raw data were analysed using Origin (Pro) Version 2022. The changes in absorbance spectra of GA-CDP hybrids were recorded and analysed for their interactions with Fe^{3+}. The Benesi-Hildebrand equation was employed to calculate the binding constant, K_B.

$$\frac{1}{|A_0 - A|} = \frac{1}{|A_\alpha - A|} + \frac{1}{|A_\alpha - A| K_B [Q]}$$

where, K_B is the binding or association constant, and A_0 and Aα represent the peak absorbance of GA-CDP hybrids in the absence and presence of the highest concentration of Fe^{3+} (15 μM). The dissociation constant, K_D was elucidated as the reciprocal of K_B.

2.5. Isothermal titration calorimetry (ITC) measurements

ITC measurements were carried out using a Malvern MicroCal-PEAQ ITC instrument. Solutions of GA-CDP hybrids and $FeCl_3$ were prepared in HEPES buffer (10 mM, pH 7.4). A spinning syringe was used to inject 26 consecutive 1.5 μL aliquots of Fe^{3+} into the solution of compounds to ensure continuous mixing. The reference power and temperature of the ITC cell were set at 5 cal/s and 25 °C, respectively. To ensure complete equilibration before the next injection, an interval of 150 s was maintained between subsequent measurements. Heat of dilution was subtracted to correct obtained isotherms. The thermodynamic parameters and K_D were calculated by nonlinear least squares fitting of the binding isotherms using a single site binding model in the MicroCal PEAQ-ITC analytical software.

2.6. $A\beta_{42}$ expression and purification

$A\beta_{42}$ plasmid construct was obtained from Prof. James S. Nowick, University of California, USA. The $A\beta_{42}$ protein was expressed and purified from *E. coli* in accordance with the protocols previously reported [36]. The $A\beta_{42}$ plasmid was transformed into E. coli BL21 strain and cultured in Luria-Bertani (LB) broth at 37 °C with continuous shaking (180 rpm) overnight in the presence of ampicillin (100 μM). 1% Primary culture was inoculated to 1 L of LB broth pre-treated with ampicillin, incubated until it reaches an optical density (OD) of 0.4-0.45. This was followed by induction with 1 mM isopropyl β-D-1-thiogalactopyranoside (IPTG), and further cultured for 4 h. Cells were pelleted by centrifugation at 7000×*g* at 4 °C and resuspended in 10 mM Tris/HCl and 1 mM EDTA in water (pH 8.0). The cells were sonicated and centrifuged at 38,000×*g* to obtain the pellet, which was later resuspended in Tris buffer containing 8 M urea. This was followed by HPLC purification and lyophilization to obtain the white $A\beta_{42}$ powder, which was characterised with MALDI and LC-MS, and stored in -80 °C until further use.

2.7. Tau expression and purification

The plasmid construct for full-length tau was procured from Dr. Sharad Gupta, IIT Gandhinagar, India, and was expressed and purified from E.coli, in accordance with the protocols previously reported [9,37]. Briefly, the tau plasmid was transformed into E. Coli BL21 strain and cultured in LB broth at 37 °C with continuous overnight shaking (180 rpm), in the presence of ampicillin (100 μM) and chloramphenicol (50 μM). Next, 1% primary culture was inoculated to 1 L of LB broth with antibiotics, incubated until it reaches OD of 0.6. This was followed by induction with 1 mM IPTG, and further cultured for 4 h. Cells were pelleted by centrifugation at 7000 rpm in 4 °C, followed by the resuspension of pellet in 20 mM phosphate buffer (pH 7.4) and boiled to remove unwanted proteins. Ni-NTA affinity column chromatography was employed to purify the supernatant containing the tau protein. Tau protein was quantified by Bradford assay, characterised by SDS-PAGE and stored in -80 °C until further use.

2.8. Fluorescent labelling of tau

Tau was tagged with NTA-Atto 647-N, which binds to its C-terminal His-tag. This was achieved by incubating tau protein (50 μM) with NTA-Atto 647-N (50 μM) for 1 h at 37 °C in phosphate buffer (pH = 7.4). After centrifugation at 12,000 rpm for 15 min, the supernatant was collected for further experiments.

2.9. Thioflavin T (ThT) fluorescence assay

The $A\beta_{42}$ peptide was dissolved in a PBS buffer (10 mM, pH = 7.4) containing 1% DMSO to prepare a stock solution with a final concentration of 10 μM. To evaluate the $A\beta_{42}$ aggregation inhibition ability of GA-CDP hybrids, thioflavin T (ThT) assay was performed. A predetermined quantity of Thioflavin T (ThT) was dissolved in filtered PBS (10 mM, pH = 7.4) to prepare a stock solution, with a working concentration at 10 μM. Freshly reconstituted $A\beta_{42}$ (10 μM) was incubated alone and with GA-CDP hybrids (10 μM) in PBS (10 mM, pH = 7.4) at 37 °C for 48 h. Consequently, ThT (10 μM) was added to the respective samples and left for 10 min incubation. To monitor the tau aggregation kinetics, tau (10 μM) was incubated with varying concentrations of the GA-CDP hybrids (10, 20, 30, 40, and 50 μM) for 48 h at a temperature of 37 °C. Arachidonic acid (AA) (185 μM) was used to induce aggregation of tau in the polymerisation buffer (20 mM PBS, 100 mM NaCl, pH 7.4, and 1 mM dithiothreitol). Finally, the extent of aggregation was measured using ThT fluorescence (λ_{ex} = 440 nm and λ_{ex} = 480 nm) in a 396 well plate using multi-well plate reader. The data was plotted and analysed by GraphPad Prism 8.0.1 software.

2.10. Monitoring the cellular uptake of GA-CDP hybrids

Cells were seeded at a density of 1,00,000 cells per well in a 6-well plate in DMEM-F12 with 10% FBS, and 1% PS and incubated at 37 °C with 5% CO_2 atmosphere for 24 h. Cells were treated with GA-CDP hybrids (10 μM) and incubated for 4 h under similar conditions. Following treatment, cells were gently rinsed with PBS and subjected to trypsinization. The trypsinized cells were collected in Eppendorf tubes and centrifuged at 2500 g for 7 min at 4 °C. The resulting pellet was gently resuspended in RIPA lysis buffer and kept for mild shaking for 30 min at 4 °C. Next, ethyl acetate was added to the solution, vigorously shaken, and the less dense organic layer was separated, concentrated using a rotary evaporator, and characterized using High-Resolution

Mass Spectrometry (HRMS).

2.11. (3-(4,5-Dimethylthiazol-2-yl)-2,5-diphenyltetrazolium bromide (MTT) assay

MTT assay was performed to access the cytotoxicity of GA-CDP hybrids in SH-SY5Y cells. 20,000 cells/well were seeded in a 96-well plate in DMEM-F12 with 10% FBS, and 1% PS and incubated at 37 °C with 5% CO_2 atmosphere for 24 h. Cells were treated with different concentrations of GA-CDP hybrids (10, 25, 50, 75 and 100 μM) and incubated for 36 h under similar conditions. This was followed by the addition of 10 μL of MTT solution (5 mg/mL) into each well and incubation for 3 h. Finally, the media was removed and 1:1 DMSO-MeOH (100 μL) was added to dissolve the precipitate. The absorbance was measured at 570 and 630 nm using a Spectramax microplate reader. The data was plotted and analysed by GraphPad Prism 8.0.1 software.

2.12. Neuronal rescue from $A\beta_{42}$/$A\beta_{42}$+Fe^{3+}-induced toxicity

SH-SY5Y cells were cultured in 96 well plate in DMEM-F12 with 10% FBS, and 1% PS and incubated at 37 °C with 5% CO_2 atmosphere for 24 h. Subsequently, the cells were subjected to low serum conditions (2.5%) before treatment with $A\beta_{42}$ or $A\beta_{42}$+Fe, with or without a fixed concentration (20 μM) of GA-CDP hybrids for 24 h. Neuronal rescue from $A\beta_{42}$ or $A\beta_{42}$+Fe^{3+}-induced toxicity was assessed using an MTT assay. Additionally, the concentration-dependent effects of **GCPH** and **GCTR** on $A\beta_{42}$ or $A\beta_{42}$+Fe-treated cells were examined under the same conditions.

2.13. Neuronal rescue from arachidonic acid (AA)-induced tau toxicity

For monitoring cellular rescue from tau-induced toxicity, tau (5 μM) was incubated in the presence of AA (185 μM) alone and in the presence of GA-CDP hybrids for 48 h at 37 °C. Post incubation, the samples were centrifuged at 12,000 rpm for 20 min, and the pellet was resuspended in polymerisation buffer (20 mM PBS, 100 mM NaCl, pH 7.4, and 1 mM dithiothreitol). SH-SY5Y cells were treated with the aggregated samples and incubated for 48 h. Subsequently, an MTT assay was conducted to assess cellular rescue from tau-induced toxicity in the presence of GA-CDP hybrids.

2.14. Neuronal rescue from Congo red (CR)-induced tau aggregates

SH-SY5Y cells were cultured in 96 well plate in DMEM-F12 with 10% FBS, and 1% PS and incubated at 37 °C with 5% CO_2 atmosphere for 24 h. Subsequently, the cells were subjected to low serum conditions (2.5%) before treatment with CR (50 μM), with or without varying concentrations of **GCTR** for 24 h. Neuronal rescue from CR-induced toxicity was assessed using an MTT assay.

2.15. 2,2-Diphenylpicrylhydrazyl (DPPH) radical scavenging assay

DPPH radical quenching assay was performed to demonstrate the radical scavenging ability (RSA) of GA-CDP hybrids, GA, 2a and 2c. DPPH (100 μM) was incubated alone or with varying concentrations of compound (0, 2.5, 5, 7.5, 10, 20 μM) in MeOH: H_2O (1:1) at 37 °C for 30 min. Absorbance was measured at 540 nm using Spectramax microplate reader, and the data was plotted and analysed using GraphPad Prism 8.0.1 software.

2.16. Fe^{3+}-ascorbate assay

To assess the redox silencing and ROS inhibition ability of GA-CDP hybrids, we performed *in vitro* Fe^{3+}-Ascorbate assay. Coumarin-3-carboxylic acid (3-CCA, 150 μM), Fe^{3+} (10 μM), GA-CDP hybrids, in the absence and presence of $A\beta_{42}$ (10 μM) were incubated independently in PBS (10 mM, pH = 7.4) at 37 °C with ascorbate (200 μM). 3-CCA was used to assess the $^{\cdot}OH$ generation which transformed from non-fluorescent to fluorescent, 7-OH-CCA (λex = 385 nm, λem = 450 nm). The fluorescence emission intensity of 7-OH-CCA was measured as a function of time using the Spectramax MicroPlate Reader and result was plotted and analysed using Origin (Pro) Version 2022.

2.17. TBARS assay for lipid peroxidation

In vitro lipid peroxidation assay was performed using α-phosphatidylcholine as a model lipid and Fe^{2+}-H_2O_2 ROS generating system. During lipid peroxidation, malondialdehyde (MDA) is commonly formed, which is used to estimate the extent of lipid peroxidation. MDA was measured using thiobarbituric acid (TBA), wherein TBA reacts with MDA to form thiobarbituric acid reactive substances (TBARS) with a characteristic absorbance at 532 nm. To a solution of Fe^{2+} (0.1 mM), α-phosphatidylcholine (10 mM), and GA-CDP hybrids (20 μM), H_2O_2 (1 mM) was added, and the samples were incubated for 30 min at 37 °C. These samples were treated with TBA, and absorbance at 532 nm was measured.

To assess lipid peroxidation in cells, SH-SY5Y cells (100,000 cells per well) were seeded in a 12-well plate and incubated for 24 h. The wells were treated with GA-CDP hybrids (**GCPH** or **GCTR**) at 20 μM in the presence of RSL3 and further incubated for 48 h at room temperature. After 48 h, the media was removed, and the plate was washed with cold PBS buffer. Cells were then scraped into 2.5% trichloroacetic acid (TCA) and centrifuged at 13,000 *g for 5 min. To 500 μL of the lysate supernatant, 400 μL of 15% TCA and 400 μL of 0.67% thiobarbituric acid (TBA) were added, followed by continuous vortexing and heating at 95 °C for 8 h. The RSL3-treated cells exhibited an intense pink coloration, which gradually decreased in the cells treated with GA-CDP hybrids. The solutions were cooled, followed by the addition of 3 mL butanol, and absorbance was recorded at 532 nm.

2.18. Intracellular ROS measurement

To demonstrate the ROS scavenging ability of our compounds in cells, 2′,7′-Dichlorofluorescin diacetate (DCFDA) assay was performed in cultured cells. SH-SY5Y cells were seeded in a 48-well plate (50,000 per well) in DMEM-F12 medium (Gibco, Invitrogen) with 10% FBS and 1% PS at 37 °C under 5% CO_2 atmosphere. The cultured media was exchanged with low serum DMEM F12 media (2.5% FBS) and incubated with DCFDA (10 μM) for 30 min. The cells were washed with PBS followed by treatment with H_2O_2 (50 μM) alone and in the presence of **GCPH** or **GCTR** (10 μM) for 4 h. The media was removed, cells were washed with PBS buffer thrice and the total fluorescence (λ_{em} = 530 nm) of the entire well (in the well plate) was measured using Spectramax microplate reader and data was plotted and analysed by GraphPad Prism 8.0.1 software.

2.19. Turbidity assay

Fe^{3+}-induced Liquid–liquid phase separation (LLPS) of tau was studied in the buffer containing 10 mM HEPES, 150 mM NaCl, 10% PEG, 0.1 mM EDTA and 2 mM DTT (pH 7.4). Fe^{3+}(150 μM) was added, along with or without GA-CDP hybrids, followed by incubation at 37 °C for 20 min. Turbidity measurements were conducted using a Spectramax microplate reader, and the data were plotted and analysed with GraphPad Prism 8.0.1 software.

2.20. Confocal microscopy

Fe^{3+}-induced LLPS of tau was studied in the buffer containing 10 mM HEPES, 150 mM NaCl, 10% PEG, 0.1 mM EDTA and 2 mM DTT (pH 7.4), in the presence of Fe^{3+} and incubated for 20 min to induce LLPS. For inhibition studies, the tau in LLPS buffer was treated with **GCTR** at

varying concentrations before the addition of Fe^{3+}, and for control, the same volume of DMSO was added. Liquid droplets formed during tau LLPS were visualized using fluorescence microscopy, employing a 1:20 M ratio of NTA-Atto 647-N-labeled to unlabelled tau protein. Samples (20 μL) were dropcasted on a glass bottom dish, covered with a microscopic cover glass, and sealed. Imaging was conducted with an Olympus FLUOVIEW 3000 microscope in DIC mode using a 63-oil immersion objective. Image analysis was performed in multiple areas and planes using ImageJ software, with mean fluorescence intensity plotted against the control and analysed in GraphPad Prism 8.0.1 software.

2.21. Dynamic light scattering (DLS)

Fe^{3+}-induced LLPS of tau was studied in the buffer containing 10 mM HEPES, 150 mM NaCl, 10% PEG, 0.1 mM EDTA and 2 mM DTT (pH 7.4), in the presence of Fe^{3+} and incubated for 20 min to induce LLPS. For inhibition studies, the tau in LLPS buffer was treated with **GCTR** at varying concentrations before the addition of Fe^{3+}. DLS measurements were analysed in the Zetasizer, Malvern Instrument.

2.22. Neuronal rescue from RSL3-induced ferroptosis

SH-SY5Y cells were cultured in 96 well plate using DMEM-F12 supplemented with 10% FBS, and 1% PS and incubated at 37 °C with 5% CO_2 atmosphere for 24 h. Subsequently, the culture media was replaced by DMEM-F12 supplemented with 2.5% FBS and 1% PS before individual treatments with RSL3 (1 μM). Concurrently, cells were treated with a fixed concentration (20 μM) of either **GCPH** or **GCTR** for an additional 30 h. MTT assay was performed to assess the neuronal rescue by GA-CDP hybrids from RSL3-induced ferroptosis. Under similar conditions, concentration-dependent effect of **GCPH** or **GCTR** on RSL3-treated cells was studied.

2.23. Mitochondrial membrane potential (MMP) measurement

SH-SY5Y cells were seeded into 96 plates in DMEM-F12 with 10% FBS, and 1% PS and incubated at 37 °C with 5% CO_2 atmosphere for 24 h. The cells were treated with RSL3 (1 μM) alone and in the presence of **GCPH** or **GCTR** (20 μM) for 24 h and treated with Rho123 (500 nM) in media for 15 min, followed by washing twice with PBS buffer. Similarly, cells were treated with $A\beta_{42}$ + Fe^{3+} (1:5) alone and in the presence of varied concentrations of **GCTR** (5, 10, and 20 μM) for 24 h followed by incubation with Rho123 (500 nM) in media for 15 min and washed twice with PBS buffer. Spectramax microplate reader was used to record fluorescence (λ_{ex} = 508 nm and λ_{em} = 528 nm), using the well-scan mode (>80 points, with 6 flashes per read). To monitor changes in MMP, the relative fluorescence of control was compared with the treatments and analysed using GraphPad Prism 8.0.1 software.

2.24. Mitochondrial ROS measurements

SH-SY5Y cells were seeded into 96 plates in DMEM-F12 with 10% FBS, and 1% PS and incubated at 37 °C with 5% CO_2 atmosphere for 24 h. The cells were treated with RSL3 (1 μM) alone and in the presence of **GCPH** or **GCTR** (20 μM) for 8 h and stained with MitoSox Red (5 μM) in PBS buffer for 15 min followed by washing with PBS buffer thrice. The fluorescence was recorded using the Spectramax microplate reader in well scan mode (>80 points, with 6 flashes per read). To monitor ROS levels, the relative fluorescence of control was compared with the treatments and analysed using GraphPad Prism 8.0.1 software.

2.25. Measurement of labile iron pool (LIP)

The cells were treated with RSL3 alone and in the presence of **GCPH** or **GCTR** followed by staining with calcein-acetomethoxy ester (CA-AM). In cells, CA-AM is hydrolysed by esterases to produce calcein (fluorophore) in the cytosol [38]. The calcein chelates with Fe^{3+}, resulting in quenching of fluorescence, which facilitates the quantification of LIP levels. In the experiment, SH-SY5Y cells were seeded onto confocal dishes in DMEM-F12 with 10% FBS, and 1% PS and incubated at 37 °C with 5% CO_2 atmosphere for 24 h. Thereafter, cells were treated with RSL3 (2 μM) alone and varying concentrations of **GCTR** (10 and 25 μM), followed by PBS buffer washing and staining with CA-AM for 20 min. Cells were washed thrice with PBS and imaged in live cell set up in FITC channel using 63x oil immersion with Leica DMi8 fluorescence microscope. Image analysis was performed in multiple areas using ImageJ software, with normalized droplet size plotted against the control and analysed in GraphPad Prism 8.0.1 software.

2.26. GPX4 enzymatic assay

Inhibitor Screening Assay Kit was purchased from Cayman Chemicals, for measuring GPX4 enzymatic activity. The test facilitates the detection of GPX4 enzymatic activity by using a coupled reaction with glutathione reductase (GR). During the reaction, GPX4 reduces hydroperoxide to produce oxidised glutathione (GSSG), which gets further recycled by GR and NADPH.

The corresponding equations is depicted herein:

$$ROOH + 2GSH \rightarrow ROH + GSSG + H_2O$$

$$GSSG + NADPH + H+ \rightarrow 2GSH + NADP+$$

The oxidation of NADPH to $NADP^+$ is marked by a reduction in absorbance at 340 nm (A_{340}) due to the consumption of NADPH in presence of GPX4 enzyme. The rate of decrease in A_{340} is directly proportional to GPX4 activity. The % inhibition or activation of GPX4 activity was calculated by the following equation,

$$\frac{(\text{Initial GPX4 enzyme activity} - \text{GPX4 activity in the presence of inhibitor or activator})}{\text{Initial GPX4 enzyme activity}} * 100$$

2.27. RSL3 induced Nrf2 translocation to the nucleus

SH-SY5Y cells were cultured in confocal dishes until the confluency reached 70%. The cells were treated with RSL3 (1 μM) independently and in the presence of **GCTR** (20 μM) and incubated for 36 h under ambient conditions. After 36 h, the cells were washed with warm PBS thrice for 5 min each, fixed with 4% PFA for 30 min, permeabilized, and blocked. They were then subjected to a 20 h incubation with a primary antibody specific to nuclear factor erythroid 2-related factor 2 (Nrf2), followed by a 1 h incubation with a secondary antibody labeled with Alexa Fluor-488 at room temperature. Subsequently, the cells were gently washed with PBS three times and stained with 4′,6-diamidino-2-phenylindole (DAPI). The fluorescence signals of Nrf2 were quantified to evaluate the nuclear-to-cytoplasmic Nrf2 ratio.

2.28. Monitoring GPX4 levels in the presence of RSL3 and Aβ+ Fe^{3+}

SH-SY5Y cells were cultured in confocal dishes until they reached a

confluency of 65%. Subsequently, the cells were incubated with **GCTR** (20 μM) alone or in combination with $A\beta_{42} + Fe^{3+}$ for a duration of 30 h. The cells were gently washed thrice with warm PBS and fixed with 4% paraformaldehyde for 15 min. This was followed by washing with PBS twice for 5 min, followed by treatment with permeation buffer (PBS with 0.1% Triton X-100) for 10 min. After removal of permeation buffer, the cells were washed thrice with PBS. Next, the fixed cells were blocked using 10% horse serum (HS) in PBS for 45 min at room temperature. The blocking solution was removed, followed by treatment with GPX4 specific primary antibody (dilution 1:200) and incubated for 16 h in 4 °C. Next, the samples were washed with PBS twice, followed by treatment with secondary antibody conjugated to Alexa Fluor-488 for 1.5 h at room temperature. The cells were gently washed again and counterstained with DAPI (1 μM) for 5 min before being imaged using a confocal microscope. Image analysis was performed in multiple areas using ImageJ software, with normalized droplet size plotted against the control and analysed in GraphPad Prism 8.0.1 software.

2.29. Partition coefficient determination

BBB permeability of a compound is predicted by assessing the partition coefficient (P). We assessed the Log P value of **GCTR**, through shake flask method. To an immiscible solution of H_2O and octanol (1:1), 10 μM of **GCTR** was added. The solution was mixed vigorously and allowed to partition into two layers, while the concentration of **GCTR** in the octanol and water layer was found to be 17 μM and 3.0 μM with a calculated Log P value of 0.75. The positive Log P value suggests probable BBB crossing ability for **GCTR**.

3. Results

3.1. Fe^{3+} chelation by GA-CDP hybrids

Fe^{3+} chelators are known for their ability to independently alleviate ferroptosis and oxidative stress in AD by suppressing the Fenton reaction triggered by excess Fe^{3+}. However, the development of dual-function Fe chelators targeting both ferroptosis and AD is still in its early stages. The GA-CDP hybrids (**GCPH**, **GCTY**, **GCTR**, and **GCLD**) were assessed for their Fe-chelating abilities by UV–visible spectroscopy studies in HEPES buffer (10 mM, pH = 7.4). In this study, all compounds exhibited a significant absorption peak at 280 nm, which shifted hypochromically upon addition of Fe^{3+} (Fig. 2A and Supplemental Figs. 1A–1C). The Benesi-Hildebrand equation yielded K_D indicating moderate affinity of **GCPH**, **GCTY**, **GCTR** and **GCLD** (78 ± 4 μM, 81 ± 5 μM, 50 ± 3 μM, and 96 ± 6 μM, respectively) for Fe^{3+}.

ITC studies revealed the Fe^{3+}-chelation ability and thermodynamic profiles of the hybrids (Supplemental Figs. 1D–1F). The isothermal titration calorimetry (ITC) binding isotherms fetched K_D values of 187 ± 37 μM, 279 ± 18 μM and 120 ± 5.7 μM for **GCPH**, **GCTY** and **GCTR**, respectively. Similarly, the changes in ΔG were found to be -4.83 kcal/mol, -6.22 kcal/mol, and -6.39 kcal/mol, respectively. Due to the inability to accurately fit the binding isotherm for **GCLD**, the extraction of the binding parameters was not feasible. Notably, the absorption and ITC studies have revealed the relatively higher potency of **GCTR** as an Fe-chelator.

3.2. Interaction of GA-CDP with $A\beta_{42}$

The accumulation and aggregation of $A\beta_{42}$ is an early event in AD pathology and targeting Aβ aggregation is a strategic therapeutic approach [39–44]. Molecular docking was performed to gain insights into the binding affinity and interaction of GA-CDP hybrids with $A\beta_{42}$ (-25.9 kJ/mol, -26.35 kJ/mol, -28.86 kJ/mol, and -25.94 kJ/mol, respectively) upon docking with $A\beta_{42}$ monomers (PDB ID: 1Z0Q from www.rscb.org) (Supplemental Fig. 2H), which signify spontaneous and favourable interactions in all cases [45]. Similarly, comparable negative ΔG values (-26.35 kJ/mol, -25.52 kJ/mol, -27.19 kJ/mol, and -23.84 kJ/mol, respectively) were observed for the fibrillar form of $A\beta_{42}$ (PDB ID: 1Z0Q and 2BEG from www.rscb.org) (Supplemental Figs. 3A–3C) [25,46]. The docking studies revealed that GA-CDP hybrids can bind to both monomeric and fibrillar forms of $A\beta_{42}$, with **GCTR** exhibiting the highest binding affinity. Analysis of the residues involved indicated that the binding of GA-CDP hybrids to $A\beta_{42}$ monomers and fibrils is facilitated by a variety of interactions, including hydrogen bonding, electrostatic, π-cation, π-sigma, and π-stacking interactions (Supplemental Figs. 3D–3G). In the case of the $A\beta_{42}$ monomer, **GCTR** displays a π-π stacked interaction with the Tyr 10 moiety, which potentially impedes di-tyrosine crosslinking and contributes to its slightly higher binding affinity compared to other compounds (Fig. 2B) [47,48]. In the context of $A\beta_{42}$ fibrils, **GCTR** binds to a distinct site compared to other GA-CDP hybrids (Fig. 2C). Aβ42 fibril formation is facilitated by a salt bridge formed between Asp 23 and Lys 28 [49]. Notably, **GCTR** forms a robust π-cation interaction with Lys 28, suggesting its potential to disrupt intramolecular salt bridge interactions in $A\beta_{42}$ fibrils, which is responsible for the observed superior $A\beta_{42}$ aggregation inhibition ability (Fig. 2D). Thioflavin-T (ThT) assay was employed to assess the efficacy of these compounds in inhibiting $A\beta_{42}$ aggregation.

3.3. Inhibition of $A\beta_{42}$/$A\beta_{42}$+ Fe^{3+} aggregation

The ThT-based fluorescent assay demonstrated that at a concentration of 20 μM, **GCPH**, **GCTY**, **GCTR**, and **GCLD** decreased $A\beta_{42}$ (10 μM) aggregation by 46%, 40%, 51%, and 10%, respectively as shown in Fig. 2E. Further analysis indicated that **GCTR** significantly inhibited the aggregation by ~21%, 37%, 52%, and 80% at concentrations of 10, 20, 30, and 50 μM, respectively. This performance superior to that of both **GCPH** and **GCTY** at equivalent concentrations (Supplemental Figs. 4A–4C). Evaluation of $A\beta_{42}$ aggregation upon in the presence of individual components like CDPs (2a, 2c), GA and their hybrids (**GCPH** and **GCTR**), aggregation inhibition of ~41%, ~42%, ~34%, ~45% and ~54%, respectively, was observed (Supplemental Fig. 4D). From this study, it is evident that **GCTR** is the most potent inhibitor of $A\beta_{42}$ aggregation.

Fe^{3+} has been known to accelerate $A\beta_{42}$ aggregation and exacerbate the associated toxicity [25,47]. **GCTR** demonstrated concentration-dependent activity against Fe^{3+}-induced $A\beta_{42}$ aggregation with 45%, 56%, 67%, and 85% inhibition at 10, 20, 30, and 50 μM, respectively (Fig. 2F). The performance of **GCTR** was superior when compared to the other hybrids (Supplemental Figs. 4E–4F). For instance, **GCPH** and **GCTY** showed inhibition of ~70% and 50%, respectively, at concentrations of 50 μM, compared to 85% by **GCTR**. Similarly, the Fe^{3+}-induced $A\beta_{42}$ aggregation inhibition in control experiment involving **2a**, **2c**, GA, **GCPH** and **GCTR** was found to be 28%, 49%, 47%, 32% and 54%, respectively (Supplemental Fig. 4G). The molecular docking and aggregation-inhibition studies emphasize the potency of **GCTR** as an effective modulator of $A\beta_{42}$ and $A\beta_{42}$+Fe^{3+} aggregation.

3.4. Modulation of $A\beta_{42}$/$A\beta_{42}$+ Fe^{3+} toxicity

The cellular uptake of GA-CDP hybrids was examined in SH-SY5Y cells using HRMS, which confirmed the ability of GA-CDP hybrids to effectively cross the cell membrane (Supplemental Figs. 5A and B). Subsequently, we meticulously assessed the cytotoxicity of GA-CDP hybrids before proceeding to evaluate their inhibitory potential against $A\beta_{42}$/$A\beta_{42}$+Fe^{3+}-induced neurotoxicity in SH-SY5Y cells. In MTT assay, **GCPH**, **GCTY** and **GCTR** showed cytocompatibility up to 100 μM in cells, while **GCLD** remained non-toxic up to 75 μM (Supplemental Figs. 6A–6D). The viability reduced to 55% in cells treated with $A\beta_{42}$ (10 μM) for 36 h. **GCPH**, **GCTY**, **GCTR**, and **GCLD** at concentrations of 20 μM rescued cells from $A\beta_{42}$ toxicity with improved viability to ~75%, 73%, 90%, and 64%, respectively (Supplemental Fig. 6E). The hybrids demonstrated a concentration-dependent activity, wherein

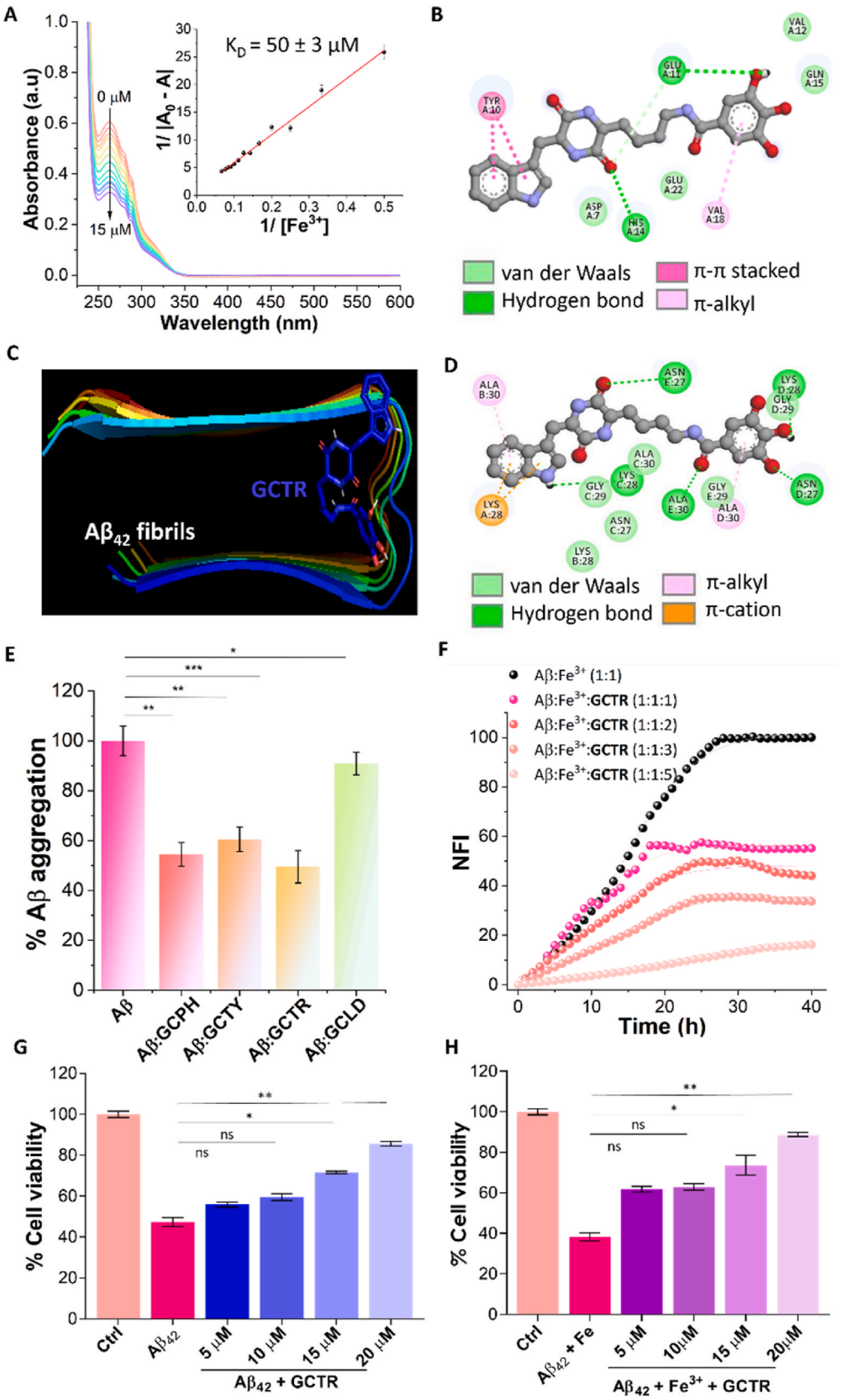

Fig. 2. Fe-chelation, *in vitro* and cellular $Aβ_{42}$/$Aβ_{42}$+Fe^{3+} aggregation inhibition and toxicity studies. (A) UV–visible spectra of **GCTR** with increasing concentrations of Fe^{3+} and binding constant derived from the plot of (1/|A_0-A|) versus 1/[Fe^{3+}] (inset) using the Benesi-Hilderbrand equation. (B-D) Interaction between **GCTR** and amino acid residues in $Aβ_{42}$ monomer (B), $Aβ_{42}$ fibril (C) and amino acid residues in $Aβ_{42}$ fibril (D) using molecular docking. (E) $Aβ_{42}$ aggregation inhibition by GA-CDP hybrids (20 μM) monitored using ThT assay. (F) Dose-dependant $Aβ_{42}$+Fe^{3+} aggregation inhibition by **GCTR** monitored using ThT assay. (G and H) Dose-dependent neuronal cell rescue by **GCTR** from $Aβ_{42}$ (G) and $Aβ_{42}$+Fe^{3+}-induced toxicity (H). [$Aβ_{42}$] = 10 μM, [$FeCl_3$] = 10 μM, [ThT] = 10 μM. Experiments repeated with n = 4, Statistical analysis: one-way ANOVA, *p = 0.05). NFI: Normalized fluorescence intensity.

GCTR significantly outperformed **GCPH** by rescuing cells from $A\beta_{42}$-induced toxicity by ~55%, 59%, 71%, and 85% at 5, 10, 15, and 20 μM, respectively (Fig. 2G and Supplemental Fig. 6F).

Next, GA-CDPs were evaluated for their ability to modulate Fe^{3+}-induced $A\beta_{42}$ toxicity. The cells incubated with $A\beta_{42}$ (10 μM) and Fe^{3+} (50 μM) for 36 h exhibited reduction in viability to 39%. Interestingly, treatment with **GCPH**, **GCTY**, **GCTR**, and **GCLD** at concentrations of 20 μM rescued the cells from $A\beta_{42}$+ Fe^{3+} toxicity with improved viability of

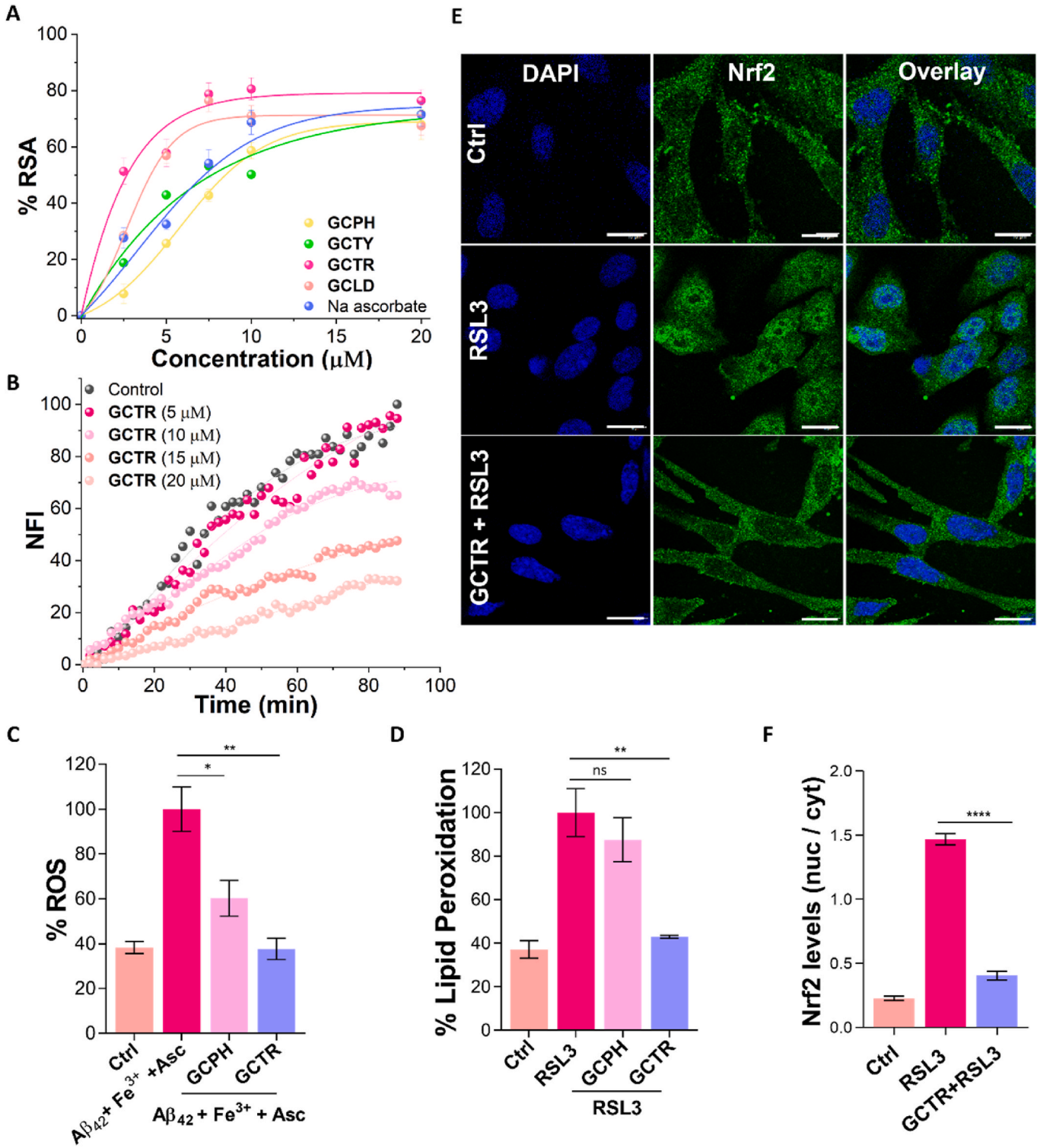

Fig. 3. *In vitro* and cellular assessment of antioxidant properties of GA-CDP hybrids. (A) DPPH assay for % RSA. (B) Fe^{3+}-ascorbate assay showing $A\beta_{42}$+Fe^{3+}-induced ROS quenching by **GCTR**. (C) DCFDA assay demonstrating the quenching of intracellular Aβ42+ Fe3+-induced ROS by **GCPH** and **GCTR**. (D) TBARS assay show the quenching of intracellular lipid peroxidation by **GCPH** and **GCTR**. [$A\beta_{42}$] = 10 μM, [Fe^{3+}] = 50 μM, and [**GCPH**] = [**GCTR**] = 20 μM. (E-F) Immunofluorescence (IF) assay to monitor RSL3 induced Nrf2 translocation to the nucleus and in the presence of **GCTR** (E) and its quantification (F). (Scale bar = 10 μm). Over 200 cells were quantified, the data between two groups were analysed by independent samples *t*-test, and one-way ANOVA was used to compare the means of three groups, *p = 0.05. RSA: Radical scavenging ability.

~78%, 62%, 95%, and 68%, respectively (Supplemental Fig. 6G). The hybrids displayed a concentration-dependent activity, wherein **GCTR** significantly outperformed other hybrids by rescuing cells from $A\beta_{42}$+ Fe^{3+}-induced toxicity by ~61%, 62%, 73%, and 90% at 5, 10, 15, and 20 μM, respectively (Fig. 2H and Supplemental Fig. 6H). The synergistic effect of **GCTR** in Fe-chelation and inhibition of $A\beta_{42}$ aggregation resulted in effectively mitigating the $A\beta_{42}$+ Fe^{3+}-induced cytotoxicity. Further to assess the possible blood brain barrier (BBB) crossing ability, we evaluated the partition coefficient (P) value for **GCTR**. The calculated positive log P value of 0.75 indicated possible BBB crossing ability of **GCTR** (Supplemental Figs. 7A and 7B).

3.5. GA-CDPs mitigate oxidative stress

The antioxidant potential of GA-CDPs was evaluated through standard radical scavenging assays. In DPPH assay, **GCPH**, **GCTY**, **GCTR**, and **GCLD** at concentrations of 10 μM exhibited radical scavenging activity (RSA) of 63%, 58%, 82%, and 71%, respectively, compared to natural antioxidant sodium ascorbate (68%) (Fig. 3A). Furthermore, a experiment involving **2a**, **2c**, GA, **GCPH**, and **GCTR** highlighted the superior RSA of **GCTR**, confirming its enhanced antioxidant potential compared to its individual components (Supplemental Fig. 8A). The Ferric-Ascorbate assay assessed the redox silencing of Fe^{3+} and ROS quenching effect of **GCPH** and **GCTR** at various concentrations (5, 10, 15, and 20 μM) in PBS buffer (10 mM, pH = 7.4) containing $FeCl_3$ (20 μM). **GCTR** notably quenched ROS by ~80% at 20 μM, surpassing **GCPH** (65%) (Supplemental Figs. 8B and 8C), indicating its ability to stabilize Fe^{3+} in a redox-dormant state. Similarly, in an experiment mimicking AD-like conditions with the presence of $A\beta_{42}$ (10 μM) and Fe^{3+}, **GCTR** effectively reduced $A\beta_{42}$+Fe^{3+}-induced ROS by ~70% (Fig. 3B). Subsequently, DCFDA assay was performed to quantify intracellular ROS levels in the presence and absence of **GCPH** and **GCTR**, as assessed by monitoring DCF fluorescence (λ_{em} = 529 nm). Treatment of cells with $A\beta_{42}$+Fe^{3+} (1:5) led to a 100% intracellular ROS generation, as compared to untreated cells (37%). Remarkably, treatment with **GCPH** and **GCTR** effectively mitigated this increase, reducing ROS levels to 60% and 38%, respectively (Fig. 3C). These observations emphasize the superior activity of **GCTR** to silence Fe^{3+} redox cycle within the $A\beta_{42}$+Fe complex and scavenge ROS production, highlighting its exceptional antioxidant property.

In the context of ferroptosis and AD conditions, Fe^{3+}-induced ROS via Fenton reaction led to lipid peroxidation. Modulating these adverse conditions is a potential therapeutic approach against ferroptosis and AD.[44] The lipid peroxidation under Fenton conditions (Fe^{2+}+H_2O_2) was monitored using α-phosphatidylcholine as a lipid model in TBARS assay. The peroxidation of α-phosphatidylcholine induced by Fe^{2+}+H_2O_2, monitored by recording absorbance at 532 nm, served as the control and set at 100%. **GCPH**, **GCTY**, **GCTR**, and **GCLD** at 20 μM reduced lipid peroxidation by ~22%, 15%, 35%, and 20%, respectively (Supplemental Fig. 8D). Subsequently, TBARS assay was performed to quantify lipid peroxidation in cells under ferroptosis conditions. On treating cells with the ferroptosis inducer RSL3, a 40% increase in lipid peroxidation was observed compared to untreated cells. Remarkably, **GCPH** and **GCTR** (20 μM) reduced lipid peroxidation by ~13% and 58%, respectively (Fig. 3D). **GCTR** exhibited an enhanced inhibitory effect in a cellular context, potentially involving mechanisms beyond radical trapping, possibly related to GPX4.

The exceptional inhibitory efficacy of **GCTR** emphasizes its capacity for Fe^{3+} chelation and its potential to counteract the detrimental effects of lipid peroxides. In ferroptosis triggered by RSL3, Nrf2 serves as a crucial regulator of redox equilibrium [48,49]. Under normal conditions, Nrf2 is bound to KEAP1 in the cytoplasm, which under oxidative stress gets translocated to the nucleus [15,39,50]. In an IF assay, **GCTR** effectively reversed RSL3-induced Nrf2 nuclear translocation, restoring its location-specific levels to untreated cells, as measured by the ratio of nucleus/cytoplasm Nrf2 levels (Fig. 3E and F). A few reports have discussed the role of RSL3 in disrupting Nrf2 activity [51], and our study demonstrated the ability of **GCTR** to alleviate RSL3-induced oxidative stress in ferroptosis.

3.6. Modulation of tau aggregation

Dual targeting strategies for both $A\beta_{42}$ and tau aggregation inhibition are sought after in AD therapy [52,53]. Therefore, the potency of GA-CDPs to target tau aggregation pathways were investigated. Molecular docking of these hybrids with tau protofibrils (PDB ID: 5O3T of www.rscb.org) showed favourable binding with calculated -ΔG values of -30.12, -31.79, -32.63, and -25.10 kJ/mol for **GCPH**, **GCTY**, **GCTR**, and **GCLD**, respectively (Fig. 4A and Supplemental Figs. 9A–9G) [9,54]. The binding site is similar for all the GA-CDPs which primarily involves interactions through hydrogen bonding and van der Waals forces. However, **GCTR** displays strong electrostatic and π-anion interactions, making it an effective tau binder as evident from its lowest ΔG value. In ThT assay, **GCTR** (20 μM) exhibited ~50% inhibition of tau (10 μM) aggregation, as compared to **GCPH** (~36%) and **GCTY** (~14%) (Fig. 4B).

Next, ThT assay was performed with tau (10 μM) and varying concentrations of **GCPH** and **GCTR** at 10, 20, 30, 40, and 50 μM, which revealed **GCTR**'s remarkable inhibition by ~26%, 52%, 74%, 84% and 95 %, respectively. **GCTR** exhibited better inhibition at 50 μM (95%) compared to **GCPH** (70%) (Fig. 4C), establishing **GCTR** as the potent tau aggregation inhibitor (Supplemental Fig. 9H). Despite earlier observations of Fe-induced Aβ aggregation, no significant impact on tau aggregation was observed during ThT assay when Fe was added at a 1:1 ratio. The pronounced inhibitory potential of **GCTR** was reinforced by ITC studies, wherein the K_D and ΔG values were found to be 9.6 μM and -31.08 kJ/mol respectively (Fig. 4D). Encouraged by strong inhibitory effects of **GCTR** on tau aggregation, its impact in cells was examined. The cells with arachidonic acid-induced tau aggregates showed reduced cell viability of ~66%. However, **GCTR** treatment at concentrations of 5, 10, and 20 μM for 48 h restored cell viability to ~85%, 88%, and 100%, respectively (Fig. 4E). This confirms the ability of **GCTR** to inhibit tau aggregation and associated cytotoxicity.

3.7. Targeting Fe^{3+}-induced tau LLPS

LLPS of tau triggers the formation of oligomeric tau species, which acts as intermediates for tau fibrillization, thus amplifying the neurotoxicity associated with AD [7,55]. A few studies have investigated the pathological role of Fe^{3+} in enhancing LLPS of tau and we assessed the effect of **GCPH** and **GCTR** on Fe^{3+}-induced tau LLPS. Initially, the turbidity was monitored in LLPS buffer (10 mM HEPES, 150 mM NaCl, 10% PEG, 0.1 mM EDTA, 2 mM DTT, pH 7.4). An increase in turbidity was observed for 50 μM Fe^{3+}, which attained saturation at 150 μM Fe^{3+}, indicating Fe^{3+}-induced LLPS of tau (Supplemental Fig. 10A). A similar experiment was performed to monitor the effect of **GCPH** and **GCTR** (20 μM) on Fe^{3+}-induced LLPS of tau. As expected, an increase in turbidity was observed in the presence of Fe^{3+} (150 μM) as compared to monomeric tau, which was found to be inhibited on co-incubation with **GCPH** and **GCTR** (Supplemental Fig. 10B). The effective concentration for the inhibition of Fe^{3+}-induced LLPS of tau was ascertained by monitoring phase separation with varying **GCTR** concentrations (0.5 to 20 μM), which showed a gradual decline in turbidity (Fig. 4F). To the best of our knowledge, **GCTR** is the one of its kind inhibitors of Fe^{3+}-induced LLPS of tau, indicating its potential in modulating tau aggregation.

The Fe^{3+}-induced LLPS of tau was visualized using Atto647-labeled tau protein using confocal microscopy. Addition of Fe^{3+} (150 μM) into labeled tau protein (5 μM) in LLPS buffer resulted in the formation of phase-separated liquid droplets, which confirmed the role of Fe^{3+} in inducing LLPS of tau (Fig. 4G). Interestingly, the samples co-incubated with **GCTR** at concentrations of 0.5, 1, 2.5, and 5 μM, exhibited a gradual decline in the formation of phase-separated liquid droplets as

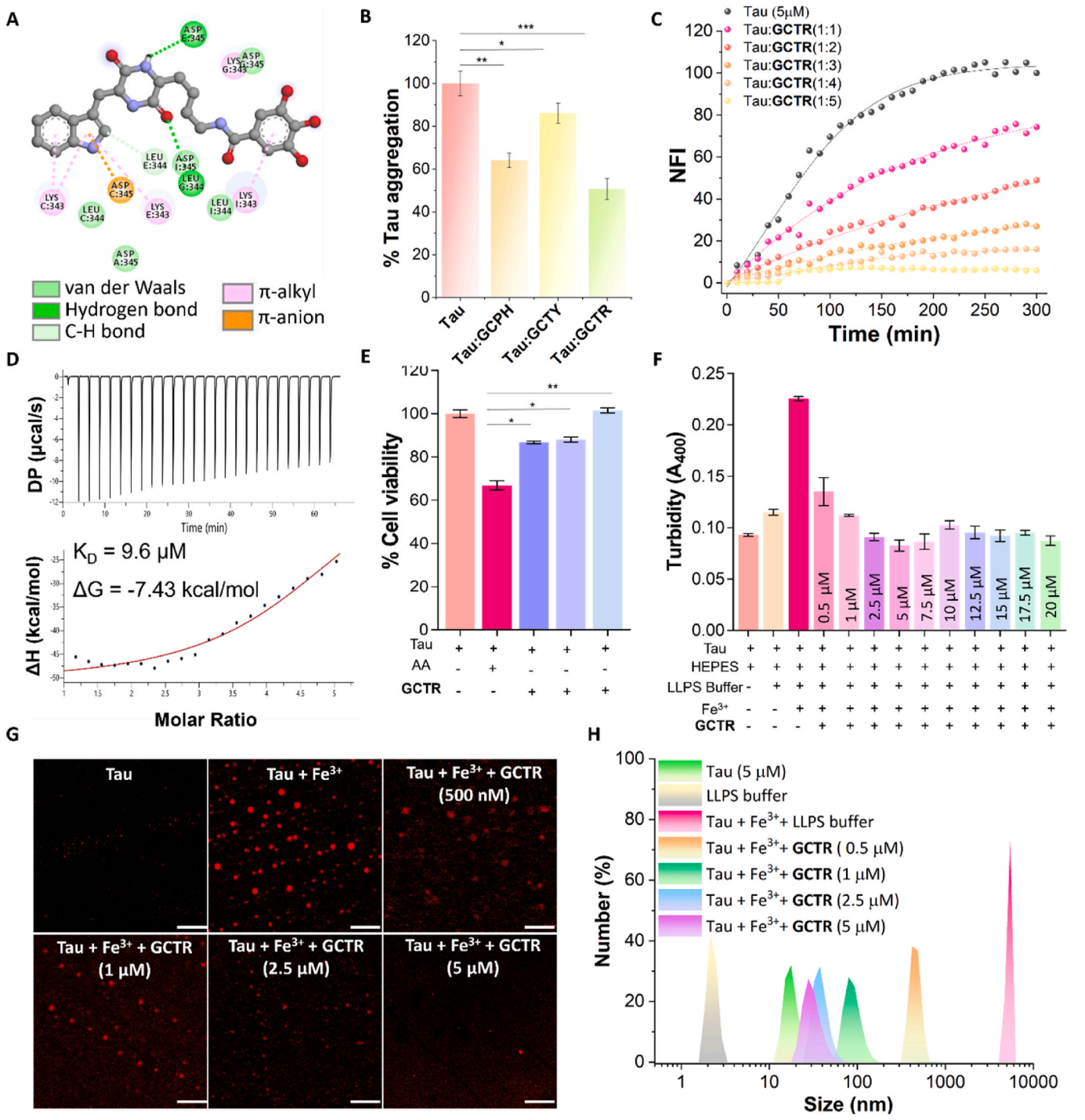

Fig. 4. Inhibition of tau aggregation and associated toxicity by GA-CDP Hybrids. (A) Interactions between **GCTR** and amino acid residues in tau protofibril, using molecular docking. (B) ThT assay shows tau aggregation inhibition by GA-CDP hybrids (20 μM). (C) Dose-dependent tau aggregation inhibition by **GCTR** monitored using ThT assay. (D) ITC studies confirm the binding affinity of **GCTR** with tau. (E) Dose-dependent neuronal cell rescue by **GCTR** from tau aggregate. (F) Dose-dependent inhibition of Fe^{3+}-induced tau LLPS by **GCTR**, using turbidity assay, and (G) confocal microscopy. (H) DLS studies monitor the inhibitory effect of **GCTR** on Fe^{3+}- induced tau LLPS. [Tau] = 10 μM, [ThT] = 10 μM, [Fe^{3+}] = 150 μM, LLPS buffer, i.e., 10 mM HEPES, 100 mM NaCl, 10% PEG. (Scale bar = 5 μm). Experiments were repeated with n = 4 and one-way ANOVA was used to compare the means of three groups, *p = 0.05.

shown in Fig. 4G, validating the inhibitory potential of **GCTR** against tau LLPS (Supplemental Fig. 10C). DLS was employed to assess the impact of **GCTR** on the size distribution during Fe^{3+}-induced LLPS of tau. As observed, incubation of tau devoid of Fe^{3+} exhibited a uniform droplet size distribution ~10 nm. However, incubation of tau with Fe^{3+} shifted the droplet size distribution to ~10 μm, indicating LLPS of tau. Interestingly, co-incubation of tau with varying concentrations of **GCTR** in the presence of Fe^{3+} and LLPS buffer resulted in a gradual decrease in the size (Fig. 4H). In the purview of monitoring aberrant tau aggregation in cells, congo red (CR) was used as an inducer of tau aggregation [56–58]. Treatment with CR (50 μM) led to a significant reduction in cell viability (~47%) compared to untreated cells. Intriguingly, co-treatment with varying concentrations of **GCTR** (5, 10, and 20 μM) restored cell viability to 66%, 73%, and 90%, respectively. This result

highlights the inhibitory ability of **GCTR** against the formation of aberrant tau aggregation in cellular contexts (Supplemental Fig. 10D). These findings highlight dual capacity of **GCTR** for Fe^{3+} chelation and tau binding, contributing to its inhibitory effects on Fe^{3+}-induced LLPS of tau and tau aggregation.

3.8. Alleviating ferroptosis in cells

The Fe^{3+}-chelation, $A\beta_{42}$ aggregation inhibition, and antioxidant potential of GA-CDPs prompted their evaluation for mitigating ferroptosis in cells. To address this, **2a**, **2c**, GA, **GCPH** and **GCTY** were evaluated for their ability to rescue SH-SY5Y cells from RSL3-induced ferroptosis. On treatment of cells with RSL3 (500 nM), the viability reduced to ~40%. However, co-incubation with **2a**, **2c**, GA, **GCPH** and **GCTY** resulted in cellular rescue of 48%, 52%, 47%, 58% and 77%, respectively, which revealed an improved inhibition of ferroptosis by **GCPH** and **GCTR**, as compared to their individual components (Supplemental Fig. 11A). Furthermore, treating cells with varying concentrations of **GCPH** and **GCTR** (10, 25, and 50 μM) revealed the excellent ability of **GCTR** to rescue cells from RSL3-induced ferroptosis, achieving ~100% cell rescue at 50 μM (Fig. 5A and Supplemental Fig. 11B). Excessive ROS in ferroptosis disrupts mitochondrial function and membrane integrity, emphasizing the importance of mitochondrial protection and redox balance for AD therapy [59]. As evidenced by Rho123 emission, treating SH-SY5Y cells with RSL3 (1 μM) reduced MMP to ~76%, while treatment with **GCPH** and **GCTR** at 20 μM restored MMP to 88% and 95%, respectively (Fig. 5B). The presence of $A\beta_{42}$ + Fe^{3+} induces significant mitochondrial changes, exacerbating

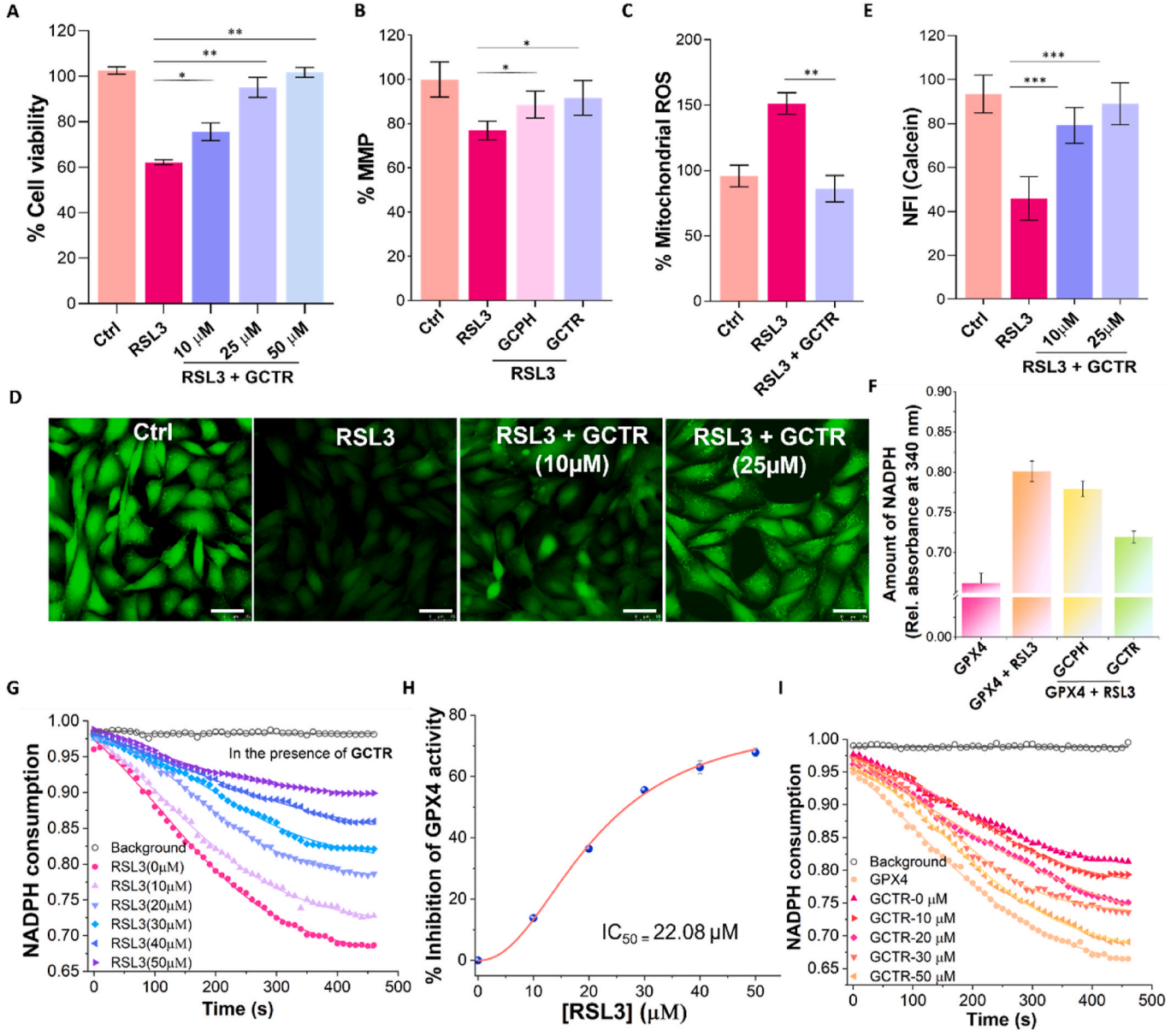

Fig. 5. Cellular studies and GPX4 enzymatic assay show GCPH and GCTR as ferroptosis inhibitors. (A) Dose-dependent neuronal cell rescue by **GCTR** from RSL3 induced toxicity. (B) Mitochondrial Membrane Potential (MMP) is monitored with **GCPH** and **GCTR**, using Rho123. (C) Intracellular mitochondrial ROS quenching by **GCTR**, using MitoSOX in RSL3-treated cells. (D and E) Monitoring labile iron pool (LIP) levels, using Calcein-AM (D) and its quantification (E) [RSL3] = 2 μM, [**GCPH**] = [**GCTR**] = 20 μM. (F) Monitoring GPX4 activity modulation in the presence of RSL3 treated with **GCPH** and **GCTR**. (G and H) Monitoring GPX4 activity on increasing concentrations of RSL3 and **GCTR** (20 μM) (G), and its IC50 plot (H). (I) Restoration of GPX4 activity in the presence of **GCTR**. (Scale bar = 25 μm). Over 200 cells were quantified, the data between two groups were analysed by independent samples *t*-test, and one-way ANOVA was used to compare the means of three groups, *p = 0.05.

oxidative stress and disrupting cellular homeostasis. Similarly, $A\beta_{42}$+Fe^{3+} treatment resulted in a reduction of MMP to 67%. Notably, the addition of **GCTR** at concentrations of 5, 10, and 20 μM effectively restored MMP to 80%, 89%, and 95%, respectively (Supplementary Fig. 10C). These findings underscore the promising effect of **GCTR** in preserving mitochondrial health. Similarly, MitoSox was used to measure the mitochondrial ROS levels under ferroptosis. Treating cells with RSL3 (1 μM) increased mitochondrial ROS levels by ~1.5 times as compared to untreated cells (100%). However, treatment with **GCTR** (20 μM) completely reduced ROS levels, making them comparable to those of untreated cells (Fig. 5C). These findings emphasize the potential of **GCTR** in preserving mitochondrial integrity during ferroptosis. Elevated labile iron pool (LIP) in ferroptosis exacerbates oxidative stress and lipid peroxidation, thereby intensifying the pathogenesis [60].

To measure LIP in ferroptosis, we employed a cell-based assay with the Fe chelator calcein-AM (CA-AM), utilizing calcein (CA) fluorescence as quantitative measure of cellular free Fe levels. Cells treated with RSL3 (2 μM) exhibited reduced CA fluorescence (48%) compared to healthy cells (100%). However, co-treatment with **GCTR** at 5, 10, and 20 μM concentrations gradually restored CA fluorescence, highlighting the effectiveness of **GCTR** in arresting excessive LIP due to its excellent Fe-chelating property (Fig. 5D and E). Cumulatively, these results affirm **GCTR** as an effective inhibitor of ferroptosis.

3.9. GCTR restores GPX4 activity

In ferroptosis and AD conditions, the activity and levels of GPX4 are compromised [61,62]. Thus, we monitored the effect of GA-CDPs (**GCPH** and **GCTR**) on the enzymatic activity of GPX4 by utilizing the GPX4 Inhibitor Screening Assay Kit (Cayman Chemical, USA). A reference kinetic curve for GPX4 activity was established through a gradual decline in absorbance over time. In the presence of RSL3 (20 μM) GPX4 activity reduced by ~22%, which is in accordance with the previous reports from literature [25]. It is noteworthy that **GCPH** and **GCTR** (20 μM) reversed this inhibition by 2.7% and 10.1% respectively (Supplemental Fig. 11D), suggesting the significant modulatory activity of **GCTR** (Fig. 5F).

Next, we performed concentration-dependent inhibition of RSL3-induced GPX4 activity by RSL3, which revealed IC_{50} of 12.42 μM (Supplemental Figs. 11E and 11F). In the presence of **GCTR** (20 μM), the IC_{50} of RSL3 increased to 22.08 μM (Fig. 5G) indicating a ~29% reduction in GPX4 inhibition (Fig. 5H). Further, a concentration-dependent study (10 to 50 μM) demonstrated a significant restoration of GPX4 activity at 50 μM of **GCTR**, highlighting its potency to restore GPX4 function against the harmful effects of RSL3 (Fig. 5I). Therefore, **GCTR** emerged as a trojan horse, alleviating the pathological features of ferroptosis by restoring GPX4 enzymatic activity and protecting cells from RSL3-induced toxicity.

3.10. GCTR enhances GPX4 levels

Ferroptosis induced by $A\beta_{42}$+Fe^{3+} results in elevated ROS production, lipid peroxidation, and neuronal impairment. We evaluated the influence of **GCTR** on cellular GPX4 levels through IF assay and western blot analyses. The treatment of SH-SY5Y cells with $A\beta_{42}$+Fe^{3+} substantially reduced GPX4 levels to ~55% compared to healthy cells (100%), indicating the induction of ferroptosis under AD conditions. Interestingly, treating SH-SY5Y cells under $A\beta_{42}$+Fe^{3+} toxicity with **GCTR** significantly enhanced GPX4 levels by ~1.55 fold, emphasizing its ability to enhance GPX4 levels in the context of AD (Fig. 6A and B). Remarkably, cells treated with **GCTR** alone also increased GPX4 levels by ~1.6 fold, reaffirming its role as a potent GPX4 enhancer in cellular contexts. To further elucidate the expression of GPX4 in presence of **GCTR**, western blot analysis was performed. The results revealed that GPX4 expression was significantly increased by ~1.68 fold, as compared to untreated cells, corroborating our earlier observations (Fig. 6C and D). These results underscore the potential of **GCTR** as a formidable enhancer of GPX4 levels, suggesting its therapeutic relevance in mitigating ferroptotic processes associated with AD. Encouraged by these observations, we investigated the influence of **GCTR** on cellular GPX4 levels in the presence of RSL3. The treatment of cells with RSL3 (1 μM) significantly reduced GPX4 levels to ~55%. However, co-treatment with **GCTR** markedly elevated GPX4 levels by ~1.5 fold compared to healthy cells (100%) (Supplemental Figs. 12A and 12B). These findings emphasize the potential of **GCTR** to enhance cellular levels of GPX4, thereby demonstrating its ability to ameliorate $A\beta_{42}$+Fe and RSL3-induced ferroptosis. This dual function positions **GCTR** as a promising modulator that addresses both ferroptosis and AD pathologies.

4. Discussion

Dyshomeostasis of Fe and its abnormal redox cycling can lead to ferroptosis, a programmed cell death pathway dependent on Fe, which is a key pathological process in many neurodegenerative diseases including AD [43,62]. The complex interplay between ferroptosis and AD presents a significant challenge, emphasizing the urgency to translate mechanistic insights into effective therapeutic strategies. Our study focuses on designing and synthesizing hybrid molecules that synergistically target ferroptosis and its ramifications in AD, exemplified by **GCTR**, a unique small molecule inhibitor. In ferroptosis, labile Fe serves a pivotal role in both enzymatic and non-enzymatic lipid peroxidation. It acts as a cofactor for lipoxygenase (LOX) enzymes, facilitating the oxidation of polyunsaturated fatty acids. Elevated Fe levels trigger the Fenton-type reaction, intensifying nonenzymatic lipid peroxidation and leading to ferroptotic cell death [63,64]. The Fe^{3+} chelation ability and antioxidant properties, of **GCTR** contribute to its excellent potency to inhibit lipid peroxidation, providing cellular defence against oxidative damage, thereby inhibiting ferroptosis. **GCTR** effectively keeps the labile iron pool (LIP) under check, and effectively mitigates lipid peroxidation in ferroptosis. $A\beta_{42}$ aggregates disrupt cellular membranes, forming pores that foster unregulated ion influx, especially Ca^{2+}, ultimately triggering cell death in AD [65]. The imbalance of Fe regulation in AD intensifies the accumulation and harmful effects of $A\beta_{42}$ aggregation. Iron binds to specific amino acid residues, including Asp, Glu, and His, within $A\beta_{42}$, which contributes to the Fenton reaction and subsequent oxidative damage and amplified $A\beta_{42}$ aggregation [66]. In this context, **GCTR** inhibits $A\beta_{42}$/$A\beta_{42}$ + Fe^{3+} aggregation, owing to its high Fe^{3+}-chelation potency. Molecular docking and residue analyses unveil its enhanced inhibitory ability fostered by π-cation interactions with Lys 28, plausibly disrupting the salt bridges involved in $A\beta_{42}$ fibrillization.

While molecules have been developed to control elevated Fe levels and lipid ROS, their success in addressing ferroptosis and AD remains limited. Notably, depletion of GPX4 activity and levels contributes to cell death under ferroptosis conditions, emphasizing the need for the development of effective GPX4 modulators. GPX4, a crucial ferroptosis regulator, fosters the conversion of toxic lipid peroxides to non-toxic lipid alcohols via system Xc-mediated GSH synthesis. The pathological nexus of ferroptosis and AD is exacerbated by reduced GPX4 levels in the presence of $A\beta_{42}$+Fe^{3+}. The exact mechanism of action for $A\beta_{42}$+Fe^{3+} reducing GPX4 levels is not fully known, but it is likely that exacerbation in oxidative stress and ferroptosis induction are involved. $A\beta_{42}$+Fe^{3+} contributes to elevated oxidative stress, substantial increase in lipid peroxidation, disruption of mitochondrial membrane and its function, which could plausibly result in depletion of GPX4 levels. **GCTR** remarkably restores GPX4 activity and enhances protein levels under AD conditions, offering a comprehensive strategy to combat ferroptosis and amyloid toxicity. The intricate regulation of GPX4 protein synthesis involves key players, including the light chain subunit solute carrier family 7 member 11 (SLC7A11)-mediated cystine uptake and the mechanistic target of rapamycin complex 1 (mTORC1). Cysteine, a crucial factor in this network, activates mTORC1, facilitating GPX4

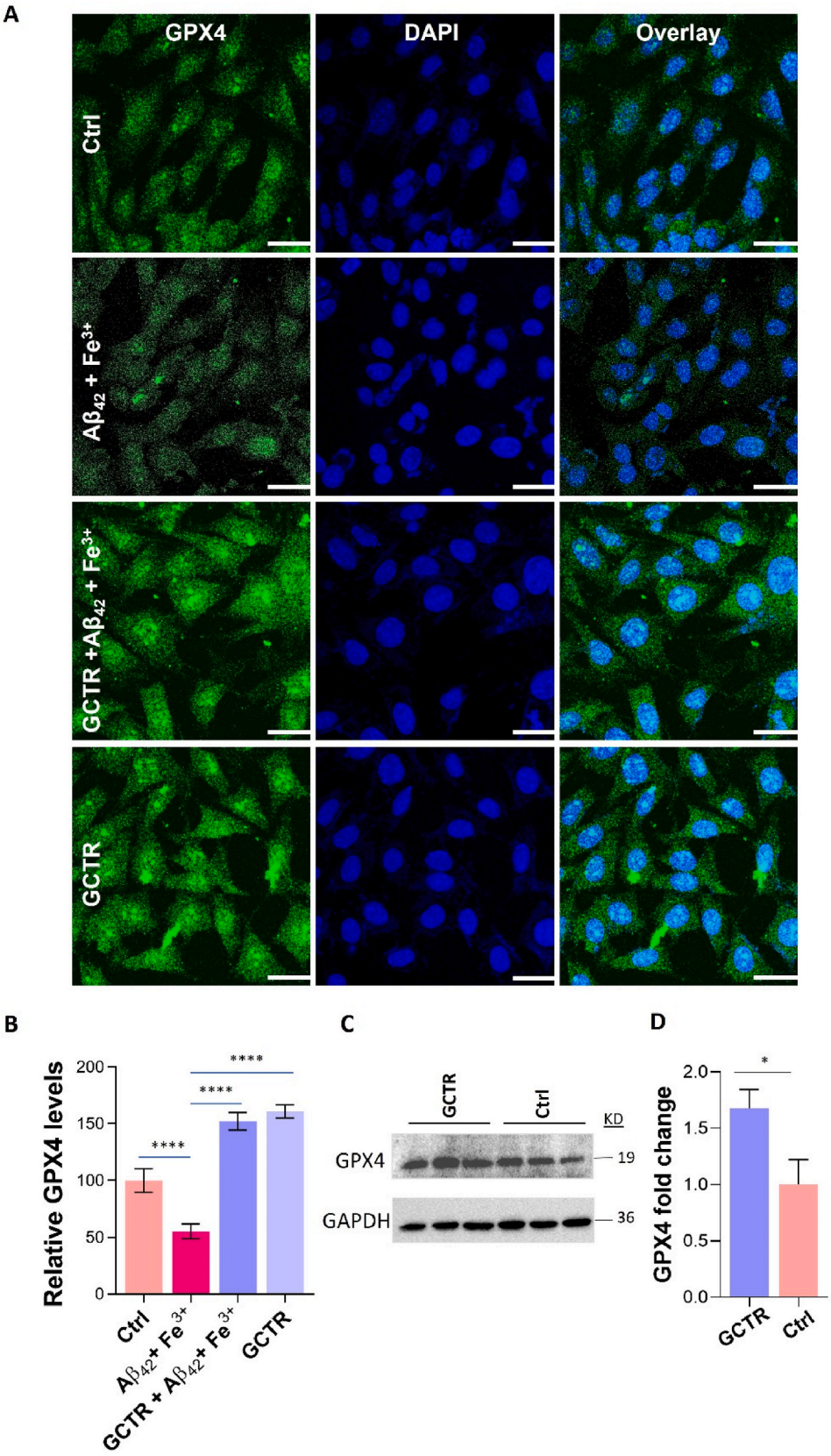

Fig. 6. GCTR enhances GPX4 cellular levels. IF study to monitor GPX4 levels in $A\beta_{42}$+Fe^{3+}-treated cells in the absence and presence of **GCTR** (A) and its quantification (B). (C) Western blot analysis to monitor the effect of **GCTR** on GPX4 levels, and its quantification (n = 3) (D). (Scale bar = 25 μm). Over 200 cells were quantified, the data between two groups were analysed by independent samples *t*-test, and one-way ANOVA was used to compare the means of three groups, *p = 0.05.

protein synthesis through the Rag-mTORC1-4EBP signalling axis [67]. Another regulatory mechanism involves upregulation of heat shock 70 kDa protein 5 (HSPA5), orchestrated by activating transcription factor 4 (ATF4), which inhibits GPX4 degradation through direct interaction [68]. While multiple pathways regulate GPX4 protein synthesis, the precise mechanism by which **GCTR** enhances GPX4 levels remains a focus for future investigations, and potential mechanisms for GPX4 enhancers are still in infancy. **GCTR**'s potential antioxidant properties play a pivotal role in mitigating the detrimental effects of excessive ROS during ferroptosis and help preserve the antioxidant potential of GPX4. By neutralizing surplus ROS, **GCTR** provides overall cellular defence against oxidative stress and prevents GPX4 degradation during ferroptosis. Enhancers of GPX4 may foster cysteine uptake, support system Xc-mediated glutathione (GSH) synthesis, a critical factor in GPX4 synthesis [69]. The regulatory role of acetyl-CoA carboxylase (ACC) in GPX4 enzymatic degradation suggests that GPX4 enhancers may operate through ACC inhibition [70]. Additionally, influencing the mevalonate (MVA) pathway, indirectly promotes GPX4 expression by regulating selenocysteine tRNA, vital for GPX4 synthesis [71]. Nevertheless, a deeper understanding of the metabolic underpinnings of GPX4 enhancers is necessary to harness their full pharmacological potential to tackle ferroptosis.

Intracellular phase separation of tau leads to the formation of metastable subcellular foci with high local concentrations of tau, promoting subsequent tau aggregation [55]. Dysregulated Fe^{3+} levels can enhance LLPS of tau, which lowers the critical concentration required for droplet formation and promotes tau aggregation [8]. **GCTR** has the potential to specifically target Fe^{3+}-induced LLPS of tau, effectively averting subsequent tau fibrillization and cellular toxicity. Owing to its dual capability for Fe^{3+}-chelation and tau binding, **GCTR** emerges as an innovative and effective small molecule-based therapeutic approach against tauopathies associated with AD. Combining the indole group of tryptophan with small molecules has proven effective in inhibiting $A\beta_{42}$ and tau in both *in vitro* and *in vivo* studies. Various hybrids, such as naphthoquinone-tryptophan and tryptophan-galactosylamin conjugates, have demonstrated anti-amyloidogenic properties by significantly inhibiting and disrupting preformed fibrillar aggregates [72–74]. Plausible mechanisms contributing to their inhibitory activity include disrupting β-sheet formations, metal chelation, radical scavenging, regulating cellular signalling, and stabilizing non-toxic conformations of $A\beta_{42}$ and tau. In this context, the tryptophan-based hybrid, **GCTR**, surpasses its individual components (GA and CDP) and other hybrids. **GCTR** effectively addresses the surge in LIP, quenches toxic lipid peroxides, inhibits $A\beta_{42}$ and tau aggregation, mitigates oxidative stress and mitochondrial dysfunction, enhances GPX4 levels, and prevents Fe^{3+}-induced LLPS of tau and its fibrillization. **GCTR** stands out as a first-of-its-kind small molecule-based hybrid, demonstrating focused and effective inhibition of ferroptosis and amyloid toxicity in the context of AD.

5. Conclusion

In summary, this study introduces **GCTR** as the first small hybrid molecule that dually mitigates the nuanced interplay between ferroptosis and amyloid toxicity in AD, based on its mechanism of action in restoring GPX4 activity and enhancing its cellular levels. Additionally, **GCTR** demonstrates a novel ability in ameliorating Fe^{3+}-induced LLPS of tau. In essence, **GCTR** emerges as a potent small hybrid molecule, strategically positioned to disrupt the pathological symbiosis between ferroptosis and AD. This study provides a basis for the future of innovative drug discovery, promising novel small molecule-based drugs targeting these complex pathological pathways.

CRediT authorship contribution statement

Dikshaa Padhi: Writing – review & editing, Writing – original draft, Visualization, Validation, Methodology, Investigation, Formal analysis, Data curation. **Prayasee Baruah:** Writing – review & editing, Investigation, Formal analysis, Data curation. **Madhu Ramesh:** Writing – review & editing, Investigation, Formal analysis, Data curation. **Hariharan Moorthy:** Writing – review & editing, Investigation, Formal analysis, Data curation. **Thimmaiah Govindaraju:** Writing – review & editing, Writing – original draft, Supervision, Resources, Project administration, Funding acquisition, Conceptualization.

Declaration of competing interest

We wish to confirm that there are no known conflicts of interest associated with this publication and there has been no significant financial support for this work that could have influenced its outcome.

Data availability

Data will be made available on request.

Acknowledgements

The authors thank JNCASR, DST (CEFPRA grant: IFCPAR/CEFIPRA-62T10-3), core grant (CRG/2020/004594), Science and Engineering Research Board (SERB), New Delhi, India, for the funding. DP, MR and HH thank DST, UGC and CSIR for the student fellowships.

Appendix A. Supplementary data

Supplementary data to this article can be found online at https://doi.org/10.1016/j.redox.2024.103119.

References

[1] T. Govindaraju (Ed.), Alzheimer's Disease:Recent Findings in Pathophysiology, Diagnostic and Therapeutic Modalities, The Royal Society of Chemistry, 2022.
[2] A. Association, Alzheimer's disease facts and figures, Alzheimer's Dementia 11 (2015) (2015) 332–384, https://doi.org/10.1016/j.jalz.2015.02.003.
[3] C. Patterson, World Alzheimer Report 2018 - the State of the Art of Dementia Research: New Frontiers, Alzheimer's Dis. Int., London, UK, 2018, pp. 1–48, https://doi.org/10.1111/j.0033-0124.1950.24_14.x.
[4] C. Cheignon, M. Tomas, D. Bonnefont-Rousselot, P. Faller, C. Hureau, F. Collin, Oxidative stress and the amyloid beta peptide in Alzheimer's disease, Redox Biol. 14 (2018) 450–464, https://doi.org/10.1016/j.redox.2017.10.014.
[5] M. Ramesh, T. Govindaraju, Multipronged diagnostic and therapeutic strategies for Alzheimer's disease, Chem. Sci. 13 (2022) 13657–13689, https://doi.org/10.1039/d2sc03932j.
[6] R.J. Ward, F.A. Zucca, J.H. Duyn, R.R. Crichton, L. Zecc, The role of iron in brain ageing and neurodegenerative disorders, Lancet Neurol. 13 (2014) 1045–1060, https://doi.org/10.1016/S1474-4422(14)70117-6.
[7] N.M. Kanaan, C. Hamel, T. Grabinski, B. Combs, Liquid-liquid phase separation induces pathogenic tau conformations in vitro, Nat. Commun. 11 (2020), https://doi.org/10.1038/s41467-020-16580-3.
[8] S. Mukherjee, D. Panda, Contrasting effects of ferric and ferrous ions on oligomerization and droplet formation of tau: implications in tauopathies and neurodegeneration, ACS Chem. Neurosci. 12 (2021) 4393–4405, https://doi.org/10.1021/acschemneuro.1c00377.
[9] M. Ramesh, C. Balachandra, P. Baruah, T. Govindaraju, Cyclic dipeptide-based small molecules modulate zinc-mediated liquid–liquid phase separation of tau, J. Pept. Sci. 29 (2023), https://doi.org/10.1002/psc.3465.
[10] W.M. Babinchak, B.K. Dumm, S. Venus, S. Boyko, A.A. Putnam, E. Jankowsky, W. K. Surewicz, Small molecules as potent biphasic modulators of protein liquid-liquid phase separation, Nat. Commun. 11 (2020), https://doi.org/10.1038/s41467-020-19211-z.
[11] Z. Du, M. Li, J. Ren, X. Qu, Current strategies for modulating Aβ aggregation with multifunctional agents, Acc. Chem. Res. 54 (2021) 2172–2184, https://doi.org/10.1021/acs.accounts.1c00055.
[12] J. Kaplan, D.M. Ward, The essential nature of iron usage and regulation, Curr. Biol. 23 (2013) R642–R646, https://doi.org/10.1016/j.cub.2013.05.033.
[13] Y. Wu, S. Torabi, R.J. Lake, S. Hong, Z. Yu, P. Wu, Z. Yang, K. Nelson, W. Guo, G. T. Pawel, J. Van Stappen, X. Shao, L.M. Mirica, Y. Lu, Simultaneous Fe2+/Fe3+ imaging shows Fe3+ over Fe2+ enrichment in Alzheimer's disease mouse brain, Sci. Adv. 7622 (2023) 1–15, https://doi.org/10.1126/sciadv.ade7622.
[14] A. Gleason, A.I. Bush, Iron and ferroptosis as therapeutic targets in alzheimer ' s disease, Neurotherapeutics 18 (2021) 252–264.
[15] S.J. Dixon, K.M. Lemberg, M.R. Lamprecht, R. Skouta, E.M. Zaitsev, C.E. Gleason, D.N. Patel, A.J. Bauer, A.M. Cantley, W.S. Yang, B. Morrison, B.R. Stockwell,

Ferroptosis: an iron-dependent form of nonapoptotic cell death, Cell 149 (2012) 1060–1072, https://doi.org/10.1016/j.cell.2012.03.042.
[16] B.R. Stockwell, J.P. Friedmann Angeli, H. Bayir, A.I. Bush, M. Conrad, S.J. Dixon, S. Fulda, S. Gascón, S.K. Hatzios, V.E. Kagan, K. Noel, X. Jiang, A. Linkermann, M. E. Murphy, M. Overholtzer, A. Oyagi, G.C. Pagnussat, J. Park, Q. Ran, C. S. Rosenfeld, K. Salnikow, D. Tang, F.M. Torti, S.V. Torti, S. Toyokuni, K. A. Woerpel, D.D. Zhang, Ferroptosis: a regulated cell death nexus linking metabolism, redox biology, and disease, Cell 171 (2017) 273–285, https://doi.org/10.1016/j.cell.2017.09.021.
[17] S. Tan, D. Schubert, P. Maher, Oxytosis: a novel form of programmed cell death, Curr. Top. Med. Chem. 1 (2001) 497–506, https://doi.org/10.2174/1568026013394741.
[18] P. Maher, A. Currais, D. Schubert, Using the oxytosis/ferroptosis pathway to understand and treat age-associated neurodegenerative diseases, Cell Chem. Biol. 27 (2020) 1456–1471, https://doi.org/10.1016/j.chembiol.2020.10.010.
[19] G. Tang, Daolin, Xin Chen, Rui Kang, Kroemer, Ferroptosis : molecular mechanisms and health implications, Cell Res. 31 (2021), https://doi.org/10.1038/s41422-020-00441-1.
[20] T. Luo, Q. Zheng, L. Shao, T. Ma, L. Mao, M. Wang, Intracellular delivery of glutathione peroxidase degrader induces ferroptosis in vivo, Angew. Chem. Int. Ed. 61 (2022) e202206277, https://doi.org/10.1002/anie.202206277.
[21] G.C. Forcina, S.J. Dixon, GPX4 at the crossroads of lipid homeostasis and ferroptosis, Proteomics 19 (2019) 1800311, https://doi.org/10.1002/pmic.201800311.
[22] Y. Wang, S. Wu, Q. Li, H. Sun, H. Wang, Pharmacological inhibition of ferroptosis as a therapeutic target for neurodegenerative diseases and strokes, Adv. Sci. 2300325 (2023), https://doi.org/10.1002/advs.202300325.
[23] E. Mishima, J. Ito, Z. Wu, T. Nakamura, A. Wahida, S. Doll, W. Tonnus, P. Nepachalovich, E. Eggenhofer, M. Aldrovandi, B. Henkelmann, K. ichi Yamada, J. Wanninger, O. Zilka, E. Sato, R. Feederle, D. Hass, A. Maida, A.S.D. Mourão, A. Linkermann, E.K. Geissler, K. Nakagawa, T. Abe, M. Fedorova, B. Proneth, D. A. Pratt, M. Conrad, A non-canonical vitamin K cycle is a potent ferroptosis suppressor, Nature 608 (2022) 778–783, https://doi.org/10.1038/s41586-022-05022-3.
[24] N. Spotorno, J. Acosta-cabronero, E. Stomrud, Relationship between cortical iron and tau aggregation in Alzheimer ' s disease, Brain 143 (2020) 1341–1349, https://doi.org/10.1093/brain/awaa089.
[25] P. Baruah, H. Moorthy, M. Ramesh, D. Padhi, T. Govindaraju, A natural polyphenol activates and enhances GPX4 to mitigate amyloid-β induced ferroptosis in Alzheimer's disease, Chem. Sci. 14 (2023) 9427–9438, https://doi.org/10.1039/d3sc02350h.
[26] K. Rajasekhar, K. Mehta, T. Govindaraju, Hybrid multifunctional modulators inhibit multifaceted Aβ toxicity and prevent mitochondrial damage, ACS Chem. Neurosci. 9 (2018) 1432–1440, https://doi.org/10.1021/acschemneuro.8b00033.
[27] T. Mori, N. Koyama, T. Yokoo, T. Segawa, M. Maeda, D. Sawmiller, Gallic acid is a dual a/b -secretase modulator that reverses cognitive impairment and remediates pathology in Alzheimer mice, J. Biol. Chem. 295 (2020) 16251–16266, https://doi.org/10.1074/jbc.RA119.012330.
[28] J. Correa, V. Dominguez-arca, R.L. Reis, E. Fernandez-megia, A.R. Arau, R.A. Pires, Functional gallic acid-based dendrimers as synthetic nanotools to remodel amyloid- β -42 into noncytotoxic forms, ACS Appl. Mater. Interfaces 13 (2021) 59673–59682, https://doi.org/10.1021/acsami.1c17823.
[29] C. Balachandra, D. Padhi, T. Govindaraju, Cyclic Dipeptide : A Privileged Molecular Scaffold to Derive Structural Diversity and Functional Utility, ChemMedChem 16 (2021) 1–31, https://doi.org/10.1002/cmdc.202100149.
[30] I. Bellezza, M.J. Peirce, A. Minelli, Cyclic dipeptides : from bugs to brain, Trends Mol. Med. 20 (2014) 551–558, https://doi.org/10.1016/j.molmed.2014.08.003.
[31] M. Teixidó, E. Zurita, R. Prades, T. Tarrago, E. Giralt, A novel family of diketopiperazines as a tool for the study of transport across the blood-brain barrier (BBB) and their potential use as BBB-shuttles, J. Am. Chem. Soc. 129 (2007) 11802–11813, https://doi.org/10.1007/978-0-387-73657-0_105.
[32] S. Manchineella, C. Voshavar, T. Govindaraju, Radical-scavenging antioxidant cyclic dipeptides and silk fibroin biomaterials, Eur. J. Org Chem. 2017 (2017) 4363–4369, https://doi.org/10.1002/ejoc.201700597.
[33] S. Manchineella, T. Govindaraju, Molecular self-assembly of cyclic dipeptide derivatives and their applications, Chempluschem 82 (2017) 88–106, https://doi.org/10.1002/cplu.201600450.
[34] D. Padhi, T. Govindaraju, Mechanistic insights for drug repurposing and the design of hybrid drugs for alzheimer's disease, J. Med. Chem. 65 (2022) 7088–7105, https://doi.org/10.1021/acs.jmedchem.2c00335.
[35] C. Balachandra, T. Govindaraju, Cyclic dipeptide-guided aggregation-induced emission of naphthalimide and its application for the detection of phenolic drugs, J. Org. Chem. 85 (2020) 1525–1536, https://doi.org/10.1021/acs.joc.9b02580.
[36] P. Prakash, T.C. Lantz, K.P. Jethava, G. Chopra, Rapid, refined, and robust method for expression, purification, and characterization of recombinant human amyloid beta 1-42, Methods Protoc 2 (2019) 1–16, https://doi.org/10.3390/mps2020048.
[37] V.G. Krishnakumar, S. Gupta, Simplified method to obtain enhanced expression of tau protein from E . coli and one-step purification by direct boiling, Prep. Biochem. Biotechnol. 47 (2017) 530–538, https://doi.org/10.1080/10826068.2016.1275012.
[38] E. Prus, E. Fibach, The labile iron pool in human erythroid cells, Br. J. Haematol. 142 (2008) 301–307, https://doi.org/10.1111/j.1365-2141.2008.07192.x.
[39] S. Samanta, K. Rajasekhar, V. Babagond, T. Govindaraju, Small molecule inhibits metal-dependent and -independent multifaceted toxicity of alzheimer's disease, ACS Chem. Neurosci. 10 (2019) 3611–3621, https://doi.org/10.1021/acschemneuro.9b00216.
[40] S. Samanta, K. Rajasekhar, M. Ramesh, N.A. Murugan, S. Alam, D. Shah, J. P. Clement, T. Govindaraju, Naphthalene monoimide derivative ameliorates amyloid burden and cognitive decline in a transgenic mouse model of alzheimer's disease, Adv. Ther. 4 (2021) 1–40, https://doi.org/10.1002/adtp.202000225.
[41] D. Padhi, C. Balachandra, M. Ramesh, T. Govindaraju, Multifunctional molecules with a bipyridyl core ameliorate multifaceted amyloid toxicity, Chem. Commun. 58 (2022) 288–6291, https://doi.org/10.1039/d2cc01168a.
[42] M. Ramesh, C. Balachandra, P. Andhare, T. Govindaraju, Rationally designed molecules synergistically modulate multifaceted Aβ toxicity, microglial activation, and neuroinflammation, ACS Chem. Neurosci. 13 (2022) 2209–2221, https://doi.org/10.1021/acschemneuro.2c00276.
[43] L. Huang, D.B. McClatchy, P. Maher, Z. Liang, J.K. Diedrich, D. Soriano-Castell, J. Goldberg, M. Shokhirev, J.R. Yates, D. Schubert, A. Currais, Intracellular amyloid toxicity induces oxytosis/ferroptosis regulated cell death, Cell Death Dis. 11 (2020), https://doi.org/10.1038/s41419-020-03020-9.
[44] M. Rana, H. Cho, T. Kanchan, L.M. Mirica, A.K. Sharma, Azo-dyes based small bifunctional molecules for metal chelation and controlling amyloid formation, Inorg. Chim. Acta. 471 (2018) 419–429, https://doi.org/10.1016/j.ica.2017.11.029.
[45] M. Konar, D. Ghosh, S. Samanta, T. Govindaraju, Combating amyloid-induced cellular toxicity and stiffness by designer peptidomimetics, RSC Chem. Biol. 3 (2022) 220–226, https://doi.org/10.1039/d1cb00235j.
[46] M. Deleanu, J.F. Hernandez, L. Cipelletti, J.P. Biron, E. Rossi, M. Taverna, H. Cottet, J. Chamieh, Unraveling the speciation of β-amyloid peptides during the aggregation process by taylor dispersion analysis, Anal. Chem. 93 (2021) 6523–6533, https://doi.org/10.1021/acs.analchem.1c00527.
[47] K. Joppe, A.E. Roser, F. Maass, P. Lingor, The contribution of iron to protein aggregation disorders in the central nervous system, Front. Neurosci. 13 (2019) 1–11, https://doi.org/10.3389/fnins.2019.00015.
[48] M. Dodson, R. Castro-Portuguez, D.D. Zhang, NRF2 plays a critical role in mitigating lipid peroxidation and ferroptosis, Redox Biol. 23 (2019) 101107, https://doi.org/10.1016/j.redox.2019.101107.
[49] T. Nguyen, P. Nioi, C.B. Pickett, The Nrf2-antioxidant response element signaling pathway and its activation by oxidative stress, J. Biol. Chem. 284 (2009) 13291–13295, https://doi.org/10.1074/jbc.R900010200.
[50] A. Anandhan, M. Dodson, C.J. Schmidlin, P. Liu, D.D. Zhang, Breakdown of an ironclad defense system: the critical role of NRF2 in mediating ferroptosis, Cell Chem. Biol. 27 (2020) 436–447, https://doi.org/10.1016/j.chembiol.2020.03.011.
[51] Z. Fan, A. Wirth, D. Chen, C.J. Wruck, M. Rauh, M. Buchfelder, N. Savaskan, Nrf2-Keap1 pathway promotes cell proliferation and diminishes ferroptosis, Oncogenesis 6 (2017) e371, https://doi.org/10.1038/oncsis.2017.65.
[52] Y. Zhang, H. Chen, R. Li, K. Sterling, W. Song, Amyloid β -based therapy for Alzheimer ' s disease : challenges , successes and future, Signal Transduct. Targeted Ther. 8 (2023) 248, https://doi.org/10.1038/s41392-023-01484-7.
[53] M. Ramesh, A. Acharya, N.A. Murugan, H. Ila, T. Govindaraju, Thiophene-based dual modulators of A β and tau aggregation, Chembiochem 22 (2021) 3348–3357, https://doi.org/10.1002/cbic.202100383.
[54] L.S. Stelzl, L.M. Pietrek, A. Holla, J. Oroz, M. Sikora, J. Köfinger, B. Schuler, M. Zweckstetter, G. Hummer, Global structure of the intrinsically disordered protein tau emerges from its local structure, JACS Au 2 (2022) 673–686, https://doi.org/10.1021/jacsau.1c00536.
[55] S. Wegmann, B. Eftekharzadeh, K. Tepper, K.M. Zoltowska, R.E. Bennett, S. Dujardin, P.R. Laskowski, D. MacKenzie, T. Kamath, C. Commins, C. Vanderburg, A.D. Roe, Z. Fan, A.M. Molliex, A. Hernandez-Vega, D. Muller, A. A. Hyman, E. Mandelkow, J.P. Taylor, B.T. Hyman, Tau protein liquid–liquid phase separation can initiate tau aggregation, EMBO J. 37 (2018) 1–21, https://doi.org/10.15252/embj.201798049.
[56] B. Dai, T. Zhong, Z. Chen, W. Chen, N. Zhang, X. Liu, L. Wang, J. Chen, Y. Liang, Myricetin slows liquid – liquid phase separation of Tau and activates ATG5-dependent autophagy to suppress Tau toxicity, J. Biol. Chem. 297 (2021) 101222, https://doi.org/10.1016/j.jbc.2021.101222.
[57] K. Wang, J.Q. Liu, T. Zhong, X.L. Liu, Y. Zeng, X. Qiao, T. Xie, Y. Chen, Y.Y. Gao, B. Tang, J. Li, J. Zhou, D.W. Pang, J. Chen, C. Chen, Y. Liang, Phase separation and cytotoxicity of tau are modulated by protein disulfide isomerase and S-nitrosylation of this molecular chaperone, J. Mol. Biol. 432 (2020) 2141–2163, https://doi.org/10.1016/j.jmb.2020.02.013.
[58] X. Liu, J. Hu, M. Hu, Y. Zhang, Z. Hong, X. Cheng, J. Chen, D. Pang, Y. Liang, Sequence-dependent abnormal aggregation of human Tau fragment in an inducible cell model, BBA - Mol. Basis Dis. 1852 (2015) 1561–1573, https://doi.org/10.1016/j.bbadis.2015.04.015.
[59] A. Misrani, S. Tabassum, L. Yang, Mitochondrial dysfunction and oxidative stress in alzheimer ' s disease, Front. Aging Neurosci. 13 (2021) 1–20, https://doi.org/10.3389/fnagi.2021.617588.
[60] Y. Wu, S.F. Torabi, R.J. Lake, S. Hong, Z. Yu, P. Wu, Z. Yang, K. Nelson, W. Guo, G. T. Pawel, J. Van Stappen, X. Shao, L.M. Mirica, Y. Lu, Simultaneous Fe2+/Fe3+ imaging shows Fe3+ over Fe2+ enrichment in Alzheimer's disease mouse brain, Sci. Adv. 9 (2023) 1–15, https://doi.org/10.1126/sciadv.ade7622.
[61] W.S. Yang, B.R. Stockwell, Synthetic lethal screening identifies compounds activating iron-dependent, nonapoptotic cell death in oncogenic-RAS-harboring cancer cells, Chem. Biol. 15 (2008) 234–245, https://doi.org/10.1016/j.chembiol.2008.02.010.
[62] X. Sui, R. Zhang, S. Liu, T. Duan, L. Zhai, M. Zhang, X. Han, Y. Xiang, X. Huang, H. Lin, T. Xie, RSL3 drives ferroptosis through GPX4 inactivation and ros production in colorectal cancer, Front. Pharmacol. 9 (2018) 1–8, https://doi.org/10.3389/fphar.2018.01371.

[63] J. Li, F. Cao, H. liang Yin, Z. jian Huang, Z. tao Lin, N. Mao, B. Sun, G. Wang, Ferroptosis: past, present and future, Cell Death Dis. 11 (2020) 88, https://doi.org/10.1038/s41419-020-2298-2.

[64] A. Ashraf, P. So, Spotlight on ferroptosis : iron-dependent cell death in alzheimer ' s disease, Front. Aging Neurosci. 12 (2020) 1–10, https://doi.org/10.3389/fnagi.2020.00196.

[65] L. Pedrera, R.A. Espiritu, U. Ros, J. Weber, A. Schmitt, J. Stroh, S. Hail, S. Von Karstedt, A.J. García-sáez, Ferroptotic pores induce Ca 2 + fl uxes and ESCRT-III activation to modulate cell death kinetics, Cell Death Differ. 28 (2021) 1644–1657, https://doi.org/10.1038/s41418-020-00691-x.

[66] F. Bousejra-elgarah, C. Bijani, Y. Coppel, P. Faller, C. Hureau, Iron(II) binding to amyloid-β, the alzheimer's peptide, Inorg. Chem. 50 (2011) 9024–9030.

[67] Y. Zhang, R. V Swanda, L. Nie, X. Liu, C. Wang, H. Lee, G. Lei, C. Mao, P. Koppula, W. Cheng, J. Zhang, Z. Xiao, L. Zhuang, B. Fang, J. Chen, S. Qian, B. Gan, mTORC1 couples cyst(e)ine availability with GPX4 protein synthesis and ferroptosis regulation, Nat. Commun. 12 (2021), https://doi.org/10.1038/s41467-021-21841-w.

[68] S. Zhu, Q. Zhang, X. Sun, H.J.Z. Iii, M.T. Lotze, R. Kang, D. Tang, HSPA5 regulates ferroptotic cell death in cancer cells, Cancer Reserach 77 (2017) 2064–2077, https://doi.org/10.1158/0008-5472.CAN-16-1979.

[69] L. Liu, N. Lian, L. Shi, Z. Hao, K. Chen, Ferroptosis : mechanism and connections with cutaneous diseases, Front. Cell Dev. Biol. 10 (2023) 1–16, https://doi.org/10.3389/fcell.2022.1079548.

[70] K. Shimada, R. Skouta, A. Kaplan, W.S. Yang, M. Hayano, S.J. Dixon, L.M. Brown, C.A. Valenzuela, A.J. Wolpaw, B.R. Stockwell, Metabolic regulation of ferroptosis, Nat. Chem. Biol. 12 (2016), https://doi.org/10.1038/nchembio.2079.

[71] G.J. Warner, M.J. Berry, M.E. Moustafa, B.A. Carlson, D.L. Hatfield, J.R. Faust, Inhibition of selenoprotein synthesis by selenocysteine tRNA [ser] sec lacking isopentenyladenosine, J. Biol. Chem. 275 (2000) 28110–28119, https://doi.org/10.1074/jbc.M001280200.

[72] V.G. Krishnakumar, A. Paul, E. Gazit, D. Segal, Mechanistic insights into peptide fibrils by Naphthoquinone- Tryptophan hybrids, Sci. Rep. (2018) 1–12, https://doi.org/10.1038/s41598-017-18443-2.

[73] A. Paul, M. Frenkel-pinter, D.E. Alvarez, G. Milordini, E. Gazit, E. Zacco, D. Segal, Tryptophan-galactosylamine conjugates inhibit and disaggregate amyloid fibrils of Aĩ^{2}42 and hIAPP peptides while reducing their toxicity, Commun. Biol. 3 (2020) 1–12, https://doi.org/10.1038/s42003-020-01216-5.

[74] S. Paci, E. Gazit, D. Segal, Antagonistic activity of naphthoquinone-based hybrids toward amyloids associated with alzheimer ' s disease and type - 2 diabetes. https://doi.org/10.1021/acschemneuro.9b00123, 2019.